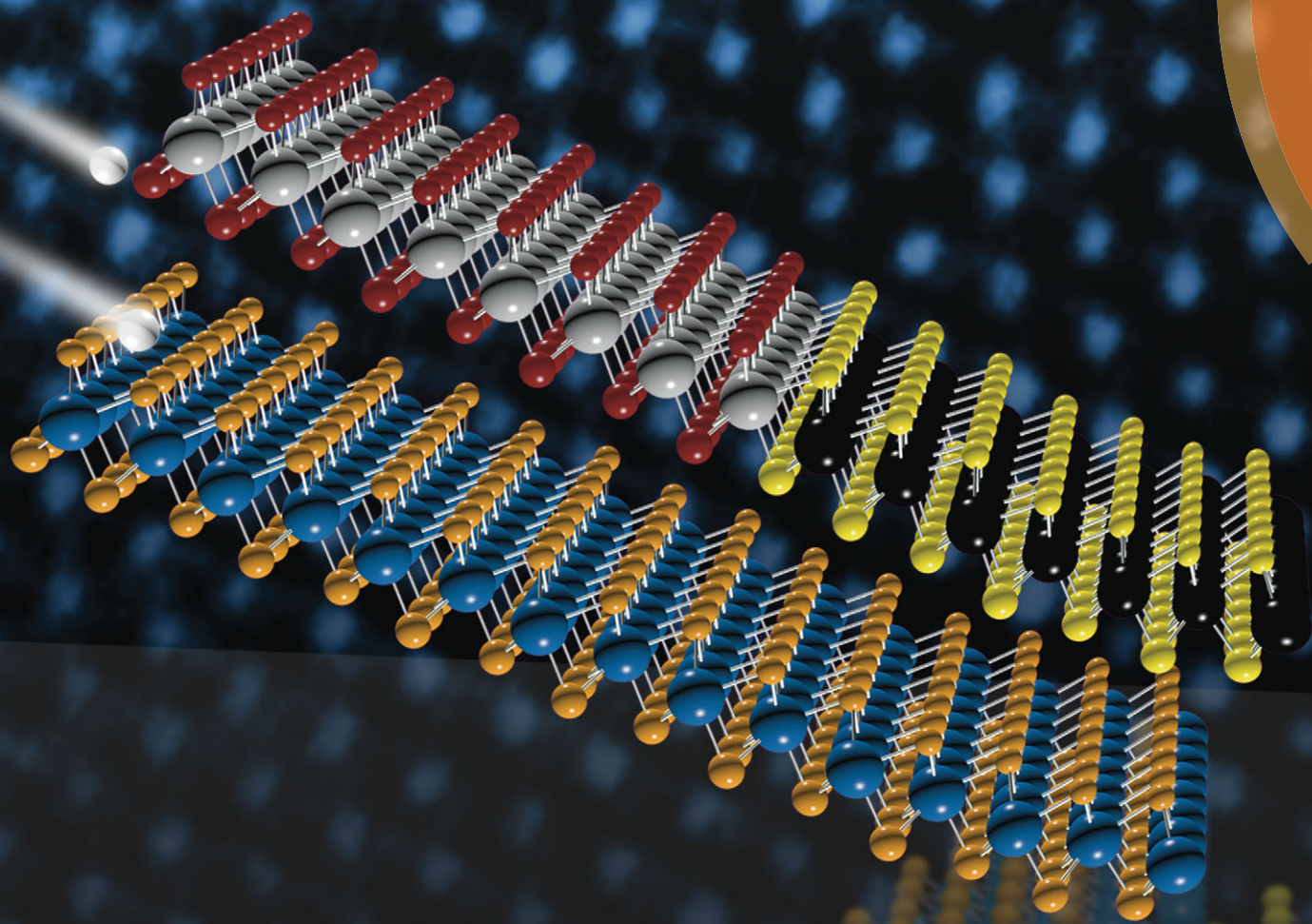


# Chem Soc Rev

Chemical Society Reviews

[www.rsc.org/chemsocrev](http://www.rsc.org/chemsocrev)



Themed issue: 2D transition metal dichalcogenide (TMD) nanosheets

ISSN 0306-0012



REVIEW ARTICLE

Yi Cui *et al.*

Physical and chemical tuning of two-dimensional transition metal dichalcogenides



Cite this: *Chem. Soc. Rev.*, 2015, 44, 2664

# Physical and chemical tuning of two-dimensional transition metal dichalcogenides

Haotian Wang,<sup>a</sup> Hongtao Yuan,<sup>abc</sup> Seung Sae Hong,<sup>a</sup> Yanbin Li<sup>b</sup> and Yi Cui<sup>\*bc</sup>

The development of two-dimensional (2D) materials has been experiencing a renaissance since the adventure of graphene. Layered transition metal dichalcogenides (TMDs) are now playing increasingly important roles in both fundamental studies and technological applications due to their wide range of material properties from semiconductors, metals to superconductors. However, a material with fixed properties may not exhibit versatile applications. Due to the unique crystal structures, the physical and chemical properties of 2D TMDs can be effectively tuned through different strategies such as reducing dimensions, intercalation, heterostructure, alloying, and gating. With the flexible tuning of properties 2D TMDs become attractive candidates for a variety of applications including electronics, optoelectronics, catalysis, and energy.

Received 28th August 2014

DOI: 10.1039/c4cs00287c

[www.rsc.org/csr](http://www.rsc.org/csr)

## 1. Introduction

Two-dimensional (2D) layered materials with important physical and chemical properties have been studied for decades. Since the recently successful preparation and characterization of graphene,<sup>1–3</sup> 2D materials have attracted a great deal of attention since they exhibit novel and intriguing properties with potential applications in field effect transistors, optoelectronic devices,

topological insulators, electrocatalysts, and so on.<sup>4–16</sup> In the rich family of 2D materials, layered transition metal dichalcogenides (TMDs) become the focus of fundamental research and technological applications due to their unique crystal structures, a wide range of chemical compositions, and a variety of material properties.<sup>6,7,11,12,17</sup> 2D TMDs are usually denoted MX<sub>2</sub>, where M represents a transition metal (such as Ti, V, Nb, Mo, Hf, Ta, W), and X represents the chalcogen (S, Se, and Te). Transition metals ranging from group 4 to group 10 have different numbers of d-electrons, which fill up the non-bonding d bands to different levels, resulting in varied electronic properties including insulating, semiconducting, metallic, and superconducting.<sup>11</sup> The wide range of electronic structures not only boosts the development of 2D TMD electronic and optoelectronic devices,

<sup>a</sup> Department of Applied Physics, Stanford University, Stanford, CA 94305, USA

<sup>b</sup> Department of Materials Science and Engineering, Stanford University, Stanford, CA 94305, USA. E-mail: [yicui@stanford.edu](mailto:yicui@stanford.edu)

<sup>c</sup> Stanford Institute for Materials and Energy Sciences, SLAC National Accelerator Laboratory, 2575 Sand Hill Road, Menlo Park, California 94025, USA



Haotian Wang

Haotian Wang is a graduate student in the Department of Applied Physics at Stanford University. He is currently a Stanford Interdisciplinary Graduate Fellow (SIGF). He obtained BS (2011) in Physics from the University of Science and Technology of China. He is now supervised by Prof. Yi Cui and focused on applications of low-dimensional materials in catalysis, energy storage, and electronics/optoelectronics.



Hongtao Yuan

Hongtao Yuan obtained his PhD (2007) degree from Institute of Physics, Chinese Academic of Sciences. He was a postdoc researcher (2007–2009) at Tohoku University, and a research associate (2010–2011) and an assistant professor (2011–2012) at Quantum Phase Electronics Center in the University of Tokyo. Since 2012 he has been a physics scientist research associate at Geballe Laboratory for Advanced Materials in Stanford University and at

Stanford Institute for Materials and Energy Sciences in SLAC National Accelerator Laboratory, USA.

but also facilitates the applications into catalysis due to the strong correlation between electronic and catalytic properties. In addition to chemical composition of 2D TMDs, atomic arrangements also play important roles in determining material properties. A representative atomic structure of 2D TMDs is shown in Fig. 1(a). The metals and chalcogens are covalently bonded within the molecular layers, which stack together *via* the weak van der Waals (vdW) interactions along the *z* axis to form the bulk material. The strong intra- and weak inter-layer interactions induce the high anisotropy of 2D TMDs, with properties such as facile single layer exfoliation for electronic devices.<sup>8</sup>

However, the explosive popularity of 2D TMDs does not only rely on the intrinsic material properties themselves, but highly depends on the tunable electronic and catalytic properties.<sup>6,7,17</sup> Due to the high anisotropy and unique crystal structure, the material properties of 2D TMDs can be effectively tuned in a wide regime through different methodologies including reducing

dimensions, intercalation, heterostructure, alloying, gating, pressure, and lighting as illustrated in Fig. 1. For example, the band structures are significantly changed as we thin down the 2D layers to the single-layer limit.<sup>8,15–17</sup> Another example is that through the intercalation of guest ions, the carrier densities of 2D TMDs can be tuned by multiple orders of magnitude.<sup>18</sup> Modern technologies and applications require a wide range of high-quality material properties, which can be hardly realized in a single material without any modifications. Therefore, 2D TMDs provide a great platform of tuning material properties towards desired functions, further attracting a great deal of attention and opening up opportunities for a wide range of applications.

There are a number of important studies and summaries focused on the attractive properties of 2D TMDs already,<sup>6,7,11,19–21</sup> however, the topical review of 2D TMDs' tunability has not been proposed yet. Understanding how the material properties can be tuned and how these tunable properties can be utilized becomes increasingly important. In this review, we focus on different physical and chemical strategies for tuning 2D TMDs properties, such as band structures, carrier densities, catalytic activities, optical properties. In each strategy, how the electronic and catalytic properties of 2D TMDs are modified is explained in detail, with representative applications included.



**Seung Sae Hong**

*Seung Sae Hong is currently a postdoctoral fellow in the group of Prof. Harold Y. Hwang at Stanford University. He received his BS degree in physics from Seoul National University and completed his PhD degree in applied physics from Stanford University, supervised by Prof. Yi Cui. His research interests include physics and materials science of low-dimensional materials, with an emphasis on chalcogenide and oxide 2D materials.*

## 2. Dimension tuning

### 2.1 Dimension tuning along the *z* direction

2D TMD semiconductors with tunable bandgaps through thinning down the bulk materials to few- or single-layer limits have recently become a powerful approach for electronic and optical applications.<sup>8,22–26</sup> As an example, the bulk MoS<sub>2</sub> crystal, an indirect bandgap semiconductor of 1.29 eV, consists of vdW bonded S–Mo–S layer units. Each of these stable units (referred to as a MoS<sub>2</sub> monolayer) consists of two hexagonal planes of



**Yanbin Li**

*Yanbin Li is a PhD student in the Department of Materials Science and Engineering at Stanford University supervised by Prof. Yi Cui. He received his BS degree in physics from University of Science and Technology of China in 2013. His graduate research focuses on the controlled synthesis of low-dimensional materials.*



**Yi Cui**

*Yi Cui is an Associate Professor in the Department of Materials Science and Engineering at Stanford University. He obtained BS (1998) in Chemistry from the University of Science and Technology of China, PhD (2002) from Harvard University. He was a Miller Postdoctoral Fellow at the University of California, Berkeley from 2003–2005. He holds a joint appointment in SLAC National Accelerator Laboratory. His current research is on two-dimensional layered materials, energy storage, photovoltaic, topological insulators, biology and environment. Yi Cui is an Associate Editor of Nano Letters. He founded Amprius Inc. in 2008, a company to commercialize the high-energy battery technology.*

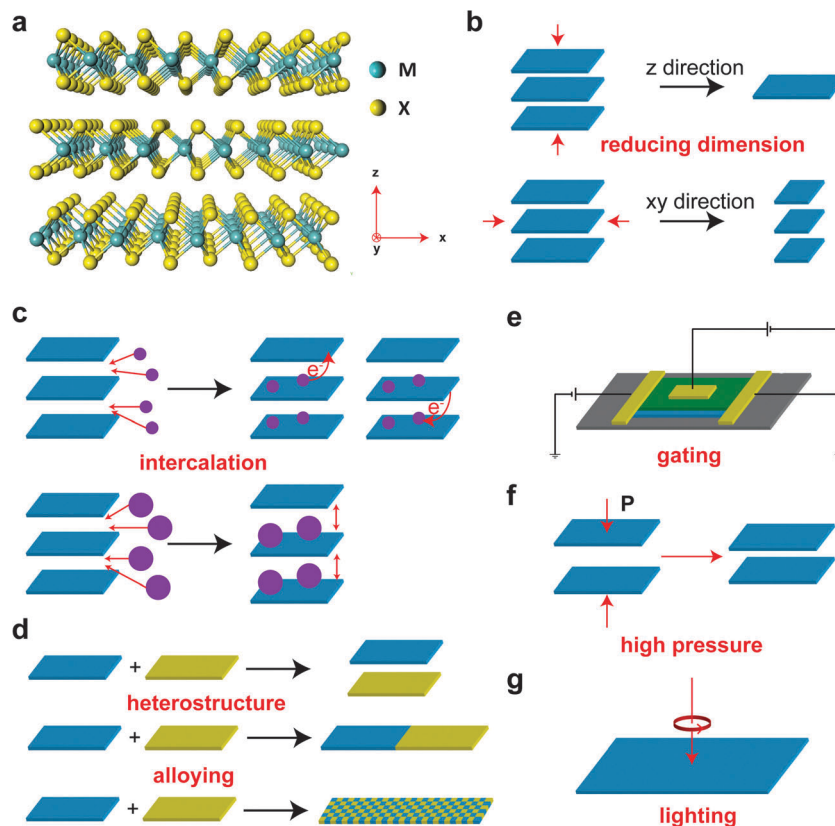


**Fig. 1** (a) Schematic of 2D TMDs. M represents a transition metal, and X represents a chalcogen. (b) Schematic of tuning 2D TMD properties by reducing dimension along the z direction and xy directions. (c) Schematic of tuning 2D TMD properties by guest ion intercalation. (d) Schematic of tuning 2D TMD properties by constructing heterostructures and alloying. (e) Schematic of tuning 2D TMD properties by gating. (f) Schematic of tuning 2D TMD properties by applying high pressure. (g) Schematic of tuning 2D TMD properties by illuminating circularly-polarized light.

S atoms and an intermediate hexagonal plane of Mo atoms coordinated through ionic-covalent interactions with the S atoms in a trigonal prismatic arrangement. Due to the high anisotropy, single-layer MoS<sub>2</sub> can be easily achieved by mechanical cleavage, directly providing the possibility to tune the physical properties at the 2D monolayer limit. Chemical vapor deposition enables large-area, uniform, and high-quality single-layer 2D TMDs.<sup>6,11,27–33</sup> In addition, chemical and electrochemical exfoliation of monolayered TMDs makes it possible to achieve large-scale single layer production.<sup>34,35</sup> As early as 2007, theorists have predicted the scaling properties in the band structure:<sup>36,37</sup> the MoS<sub>2</sub> crystals exhibit a crossover from an indirect to a direct gap semiconductor from bulk to its monolayer limit. As an early experimental report on the thickness dependent physical properties of the MX<sub>2</sub> system (Fig. 2),<sup>38,39</sup> the evolution of the electronic structure and resulting optical properties of ultrathin MoS<sub>2</sub> crystals was observed as a function of layer number from 1 to 6 layers by using spectroscopic techniques: optical absorption, photoluminescence (PL), and photoconductivity (with the thickness characterized by atomic-force microscopy). The combination of these spectroscopic methods allowed researchers to optically trace the evolution from the indirect to direct bandgaps of the material with the layer thickness decreasing to the monolayer. The crossover from an indirect gap material to a direct gap material naturally accounts for the great enhancement of the luminescence observed in

monolayer MoS<sub>2</sub>. The observed dependence of the bandgap on the layer number is also in qualitative agreement with band calculations. The controllability of the bandgap may also be used to optimize the material's use as a photocatalyst and for photovoltaic applications.

To experimentally understand the origin of these extraordinary PL properties, angle-resolved photoemission spectroscopy (ARPES) measurements are carried out to investigate the detailed parameters of the band structure and also the evolution of the band dispersion with the layer thickness (Fig. 2).<sup>40,41</sup> One example is ARPES measurement based on monolayer MoSe<sub>2</sub> thin films with variable thickness, grown by molecular beam epitaxy.<sup>40</sup> The band structure measured experimentally indicates a stronger tendency of monolayer MoSe<sub>2</sub> towards a direct bandgap. As an important feature of the monolayer MX<sub>2</sub>, a significant spin-splitting of ~180 meV at the valence band maximum of a monolayer MoSe<sub>2</sub> film, related to the strong spin orbital interaction, could be clearly observed experimentally for the first time. Other examples are observations on the evolution of the thickness-dependent electronic band structure of the MoS<sub>2</sub> and WSe<sub>2</sub>, based on the combination of the spatial resolution ARPES with the tape-cleaved or chemical-vapor-deposition-grown ultrathin samples.<sup>41</sup> All these observations provide direct evidence for indirect-to-direct band gap transition in both MoS<sub>2</sub> and WSe<sub>2</sub> cases (the shifting of the valence band maximum from *Γ* to *K*) as thinning down the sample from the bulk to monolayer.

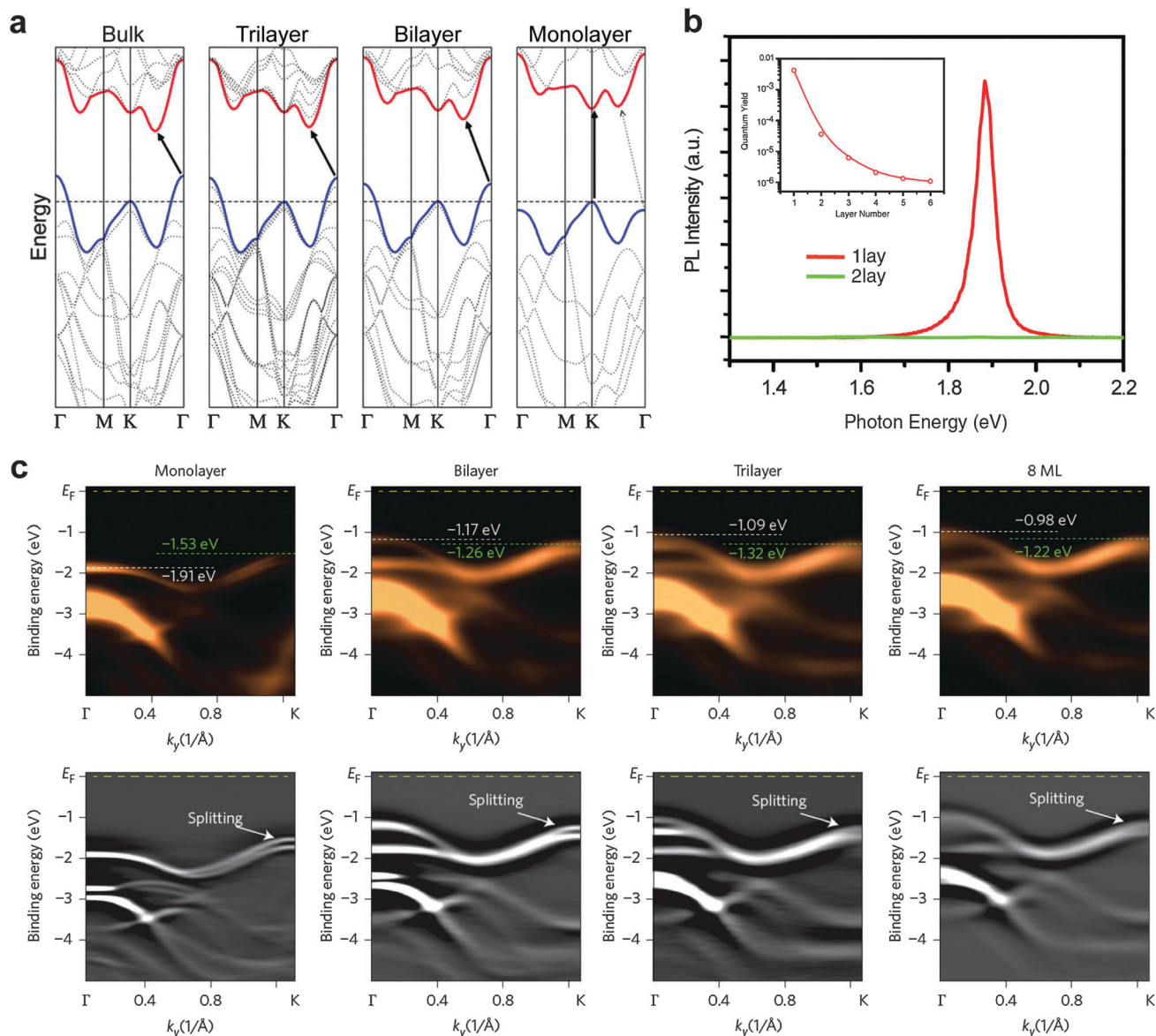


**Fig. 2** (a) Calculated band structures of bulk MoS<sub>2</sub>, quadrilayer MoS<sub>2</sub>, bilayer MoS<sub>2</sub> and monolayer MoS<sub>2</sub>. The solid arrows indicate the lowest energy transitions. Bulk MoS<sub>2</sub> is characterized by an indirect bandgap. The direct excitonic transitions occur at high energies at the K point. With reduced layer thickness, the indirect bandgap becomes larger, while the direct excitonic transition barely changes. For monolayer MoS<sub>2</sub>, it becomes a direct bandgap semiconductor. This dramatic change in electronic structure in monolayer MoS<sub>2</sub> can explain the observed jump in monolayer photoluminescence efficiency. Reproduced with permission from ref. 38. Copyright 2010, American Chemical Society. (b) PL spectra of mono- and bilayer MoS<sub>2</sub> samples in the photon energy range from 1.3 to 2.2 eV. Inset: PL quantum yield of thin layers (1–6 layers). Reproduced with permission from ref. 39. Copyright 2010, American Physical Society. (c) Band evolution with increasing thickness of MoSe<sub>2</sub> thin films. ARPES spectra and second-derivative spectra of monolayer, bilayer, trilayer and 8 ML MoSe<sub>2</sub> thin films along the  $\Gamma$ -K direction. White and green dotted lines indicate the energy positions of the apices of valence bands at the G and K points, respectively, with energy values written in the same colors. Reproduced with permission from ref. 41. Copyright 2013, Nature Publishing Group.

Such an unusual electronic structure evolution stems from the characters and spatial distribution of d-electron orbitals of MoS<sub>2</sub>. Theoretical calculations show that electronic states of different wave vectors have electron orbitals with different spatial distributions.<sup>38</sup> Specifically, conduction band states at the K point are primarily composed of strongly localized d orbitals at Mo atom sites, and they have minimal interlayer coupling since Mo atoms are located in the middle of the S–Mo–S unit cell. The states near the  $\Gamma$  point and the point of indirect band-gap originate from a linear combination of d orbitals on Mo atoms and antibonding p<sub>z</sub>

orbitals on S atoms. The orbitals have strong interlayer coupling and their energies depend sensitively on layer thickness. Such an understanding on the direct bandgap feature makes the optical measurement of the band structure available and further paves a way for the optical realization of the circularly-polarized light pumped valley polarization around the band edge at K points.

## 2.2 Dimension tuning along xy directions

Due to the highly anisotropic structures, 2D TMD materials tend to grow fast within the layer to form different morphologies such

as nanoplates, nanoribbons, nanotubes, and inorganic fullerene-like nanoparticles.<sup>27,29–31,42–44</sup> Those structures extend the dimension along the *xy* directions of 2D TMD atomic structures shown in Fig. 1(a), as an effective way to minimize the exposure of the edge sites.<sup>17</sup> However, the atomic sites on the edges of 2D TMD nanosheets have unsaturated coordination and dangling bonds, which offers interesting and important properties and applications.<sup>17,45–49</sup> By reducing the dimension along the in-plane direction, the edges of 2D TMD are largely exposed and the electronic and catalytic properties are effectively changed. Here, we choose MoS<sub>2</sub> as a typical 2D TMD material to explain the extraordinary edge properties through the *xy* dimension tuning. The edge sites of MoS<sub>2</sub> have been demonstrated to have metallic electronic states, which are absent from the basal plane.<sup>45</sup> More importantly, as illustrated in Fig. 3(a) and (b), the edge sites of MoS<sub>2</sub> are demonstrated to be active catalytic centers for hydrogen evolution reaction (HER), in sharp contrast to the HER inert terrace sites.<sup>12,47,50</sup> Other types of 2D TMDs, such as MoSe<sub>2</sub>, WS<sub>2</sub>, and WSe<sub>2</sub>, show similar edge site activities.<sup>17,51,52</sup> To make full use of the catalytic centers and enhance the HER activity, the dimension of the *xy* direction should be significantly shrunk to increase the ratio of edge sites to terrace sites. A successful example is the MoS<sub>2</sub> and MoSe<sub>2</sub> edge-terminated nanofilms shown in Fig. 3(c).<sup>17,51</sup> The TEM images show the densely packed, stripe-like grains, indicating that the molecular layers are all vertically standing on the substrate.<sup>17,51</sup> The edge-terminated surface is considered to be thermodynamically unstable due to the large surface energy of the edges; however, through rapid sulfurization synthesis, this metastable morphology is likely to be obtained by kinetically overcoming the free energy barrier.<sup>17,51</sup> The layer vertically aligned structure with reduced *xy* dimensions fully exposes the active edge sites on the substrate, providing a large number of catalytic reaction sites and thus boosting the overall HER activity.

Another way to have more active edge sites exposed is to reduce the dimension of the bulk MoS<sub>2</sub> material into ultra-small nanoparticles or nanowires.<sup>53,54</sup> The large surface curvature of the nanosized structures is likely to induce a high surface energy to force the edges to expose.<sup>55</sup> Dai and his coauthors developed a solvothermal synthesis of MoS<sub>2</sub> ultra small nanoparticles on reduced graphene oxide (RGO) sheets as illustrated in Fig. 3(d).<sup>53</sup> The particle size is only around 5 nm, exposing a large amount of edge sites. Free MoS<sub>2</sub> nanoparticles with particle size around 100 nm were also prepared for HER activity comparison with the smaller particles on RGO. The polarization curves and Tafel plots in Fig. 3(d) show that the HER performance of MoS<sub>2</sub> nanoparticles on RGO is significantly improved compared to the large sized particles. The excellent Tafel slope of 41 mV per decade indicates a facile reaction pathway with small activation barriers.<sup>53</sup> The dimensions of MoS<sub>2</sub> nanosheets along the *xy* direction can also be reduced by introducing defects into MoS<sub>2</sub> surfaces.<sup>56</sup> The defect-rich structure creates additional active edge sites in the MoS<sub>2</sub> nanosheets, significantly enhancing the HER performance with a low onset potential and a small Tafel slope. To further reduce the dimension of 2D MoS<sub>2</sub>, zero-dimension molecular MoS<sub>2</sub>,

edge site mimic is successfully prepared for high HER activity, again demonstrating the importance of edge sites.<sup>57</sup>

### 3. Intercalation tuning

#### 3.1 Intercalation tuning of electronic, optical, and thermal properties

Intercalation into layered structures changes a number of physical properties of the host materials, which has received research attention for decades.<sup>18</sup> The earlier investigations have focused on the bulk form of layered structures, and those works which are revisited as the 2D counterparts are widely studied recently. In the cases of transition metal dichalcogenides, the most common intercalants are alkali metal (Li, Na, K, ...) and 3d transition metal (V, Cr, Mn, Fe, ...) atoms, of which charges (electrons) can be easily transferred to the chalcogenide layers.<sup>19</sup> The charge transfer induced by metal atom intercalation increases the Fermi energy and density of states at the Fermi level.<sup>18</sup> Such “electron doping” results in a huge increase in carrier density – several orders of magnitude larger than the modulation by electrostatic gating and traditional impurity doping – which alters the electronic and optical properties of layered materials substantially.<sup>18,19</sup> The existence of metallic intercalants also implies that the weak interaction between layers gets stronger and the electronic structure of the whole material becomes more three-dimensional.

In addition, intercalated compounds in vdW gaps cause structural changes in the layered structure. Intercalation of organic molecules, such as *n*-octadecylamine and pyridine, is a fine example to show how the interlayer spacing between layers can be enlarged.<sup>58</sup> The increase of layer separation leads to (1) smaller bonding strength and sound velocity, and (2) the weakening of interaction among layers, which makes each layer as a nearly-isolated single layer. We introduce a few experimental examples of intercalation of layered chalcogenides, showing how structural and electronic changes make an impact on the fundamental nature of metal chalcogenides, as well as practical applications. Some of the examples, especially the optical properties, are demonstrated in two-dimensional layers, suggesting an intriguing direction for current studies of 2D materials.

Although most of the intercalation studies listed in this part are from transition metal chalcogenides, a few interesting examples can also be found in the studies of chalcogenides of non-transition metal. As their physical concepts and tuning strategy can be applied in the same way, we include those special cases as well, expecting that such conceptual approaches provide an exciting direction in transition metal chalcogenide studies.

**Thermoelectricity.** The thermoelectric effect is defined as a direct conversion between electrical energy (electric voltage) and thermal energy (temperature gradient), which is useful to extract electricity from heat, or *vice versa*. There have been a number of studies to make use of the thermoelectric effect to collect energy from waste heat, but the low efficiency of thermoelectric materials becomes a bottleneck for broad applications. One way to improve the conversion efficiency is to reduce

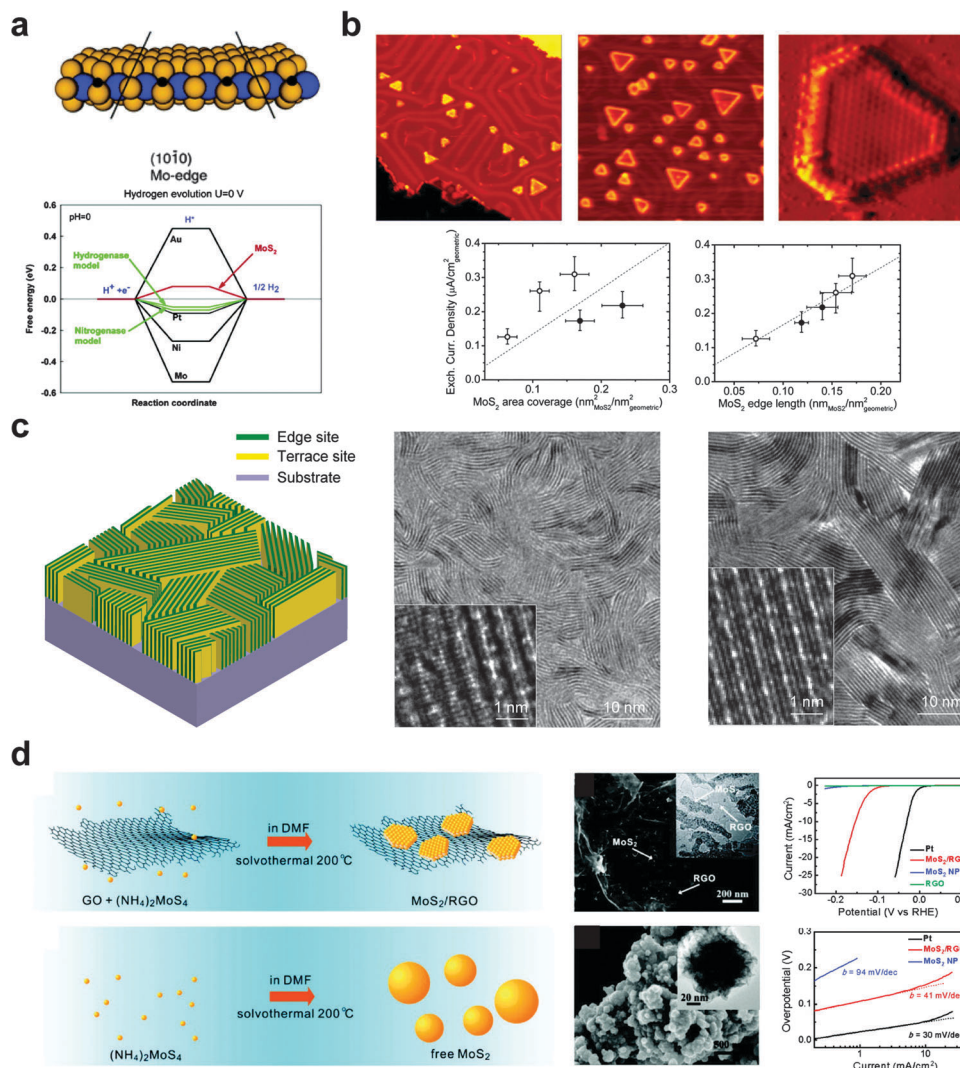


**Fig. 3** (a) Schematic of H adsorption on the MoS<sub>2</sub> Mo-edge sites (top) and theoretical simulation of the adsorption free energies on different materials (bottom). Reproduced with permission from ref. 12. Copyright 2005, American Chemical Society. (b) Experimental demonstration of the active edge site of MoS<sub>2</sub> for HER. The exchange current density scales with the length of the edges of the MoS<sub>2</sub> nanoplates. Reproduced with permission from ref. 47. Copyright 2007, the American Association for the Advancement of Science. (c) Schematic and TEM images of edge-terminated MoS<sub>2</sub> and MoSe<sub>2</sub> nanofilms. Reproduced with permission from ref. 17. Copyright 2013, American Chemical Society. (d) MoS<sub>2</sub> nanoparticles on reduced graphene oxide with excellent HER performance. Reproduced with permission from ref. 53. Copyright 2011, American Chemical Society.

thermal conductivity. Intercalation into the vdW gaps in layered structures can naturally introduce atoms/molecules to perturb phonon propagation, thereby reducing thermal conductivity. One of the earliest examples is demonstrated in non-transition metal chalcogenides, CsBi<sub>4</sub>Te<sub>6</sub>, showing how the intercalated atoms in the layered structure can help to improve the efficiency.<sup>59</sup> Cs<sup>+</sup> ions in the vdW gaps localize vibrations, generating resonant scattering of phonons. A more recent example is from the transition metal's case – titanium disulfide (TiS<sub>2</sub>). A natural superlattice of (SnS)<sub>1,2</sub>(TiS<sub>2</sub>)<sub>2</sub> is formed by intercalation of SnS layers into TiS<sub>2</sub> layered structures.<sup>60</sup> The intercalated SnS layer in the vdW gap shown in Fig. 4(a) weakens interlayer bonding, reducing the transverse sound velocity. In addition, SnS layers can function as a translational disorder in the crystal-line lattice, resulting in photon localization. Such thermal

conductivity control by intercalation is not limited to only transition metal chalcogenides but also can be generalized to other layered materials,<sup>61</sup> yielding an intriguing strategy to design thermoelectric materials made of layered structures.

**Superconductivity.** Introducing intercalants into layered structures often induces a new type of collective electronic phenomena which does not exist in the original host material. Titanium diselenide (TiSe<sub>2</sub>) exhibits charge density waves (CDWs) at low temperatures, but once Cu is intercalated (Cu<sub>x</sub>TiSe<sub>2</sub>), a new superconducting state emerges near  $x = 0.04$ , and the CDW transition is continuously suppressed as illustrated in Fig. 4(b).<sup>62</sup> Such normal-superconductor transition by intercalation has been generalized to many other types of layered materials, as shown by an emerging superconductivity *via* intercalation is Bi<sub>2</sub>Se<sub>3</sub>, a candidate material for topological insulators. It has been

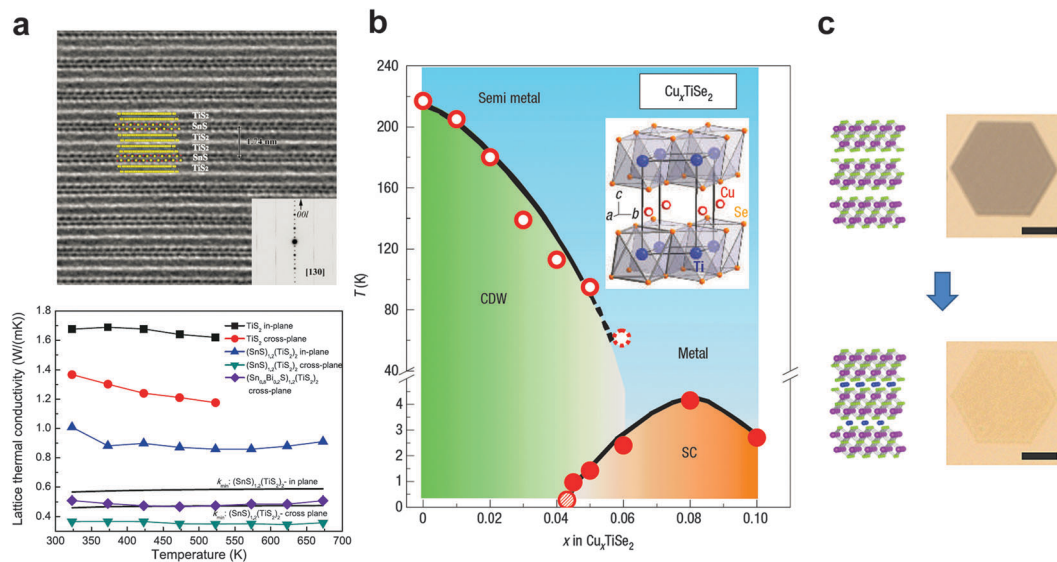


**Fig. 4** (a) Top: high-resolution transmission electron microscope (HRTEM) image of TiS<sub>2</sub> layers after SnS intercalation. Bottom: lattice thermal conductivity change by SnS intercalation. Reproduced with permission from ref. 60. Copyright 2011, Springer. (b) Phase diagram of Cu intercalated TiSe<sub>2</sub>, of which transition among metal, charge density wave (CDW), and superconductivity (SC) phases is presented. Reproduced with permission from ref. 62. Copyright 2006, Nature Publishing Group. (c) Crystal structure and optical transmission images of a Bi<sub>2</sub>Se<sub>3</sub> nanoplate before (top) and after (bottom) Cu intercalation. The scale bars indicate 4 microns. Reproduced with permission from ref. 68. Copyright 2014, Nature Publishing Group.

demonstrated that both bulk crystal synthesis<sup>63</sup> and electrochemical intercalation<sup>64</sup> of Cu can induce superconductivity in Bi<sub>2</sub>Se<sub>3</sub>. In the case of layered materials normally superconducting, intercalation can be used to enhance the superconducting transition temperature ( $T_c$ ). A well-known example of an iron-based superconductor – iron selenide (FeSe) has a  $T_c$  of 8 K. However, intercalation of metal atoms (K) and lithium amide/ammonia molecules ( $\text{Li}_x(\text{NH}_2)_y(\text{NH}_3)_{1-y}$ ) increases  $T_c$  dramatically, exceeding 30–40 K.<sup>65,66</sup> The microscopic origin of superconductivity and intercalation is not fully understood yet. Structural changes by intercalants seem to be closely related to the superconductivity, such as tetrahedral shape deformation<sup>65</sup> and increasing layer separation by the spacer layer.<sup>66</sup> Fundamental electronic parameters, such as high carrier density and the change in dimensionality of the Fermi surface, will also be important factors to explain the competition among different ground states tuned by intercalation.<sup>62</sup>

**Optical and plasmonic properties.** The large amount of metal atoms intercalated is also expected to modify optical properties of the host layered structures. Such a change in optical properties will be more evident in 2D materials, of which optical transmission and interference between interfaces can be observed by experiments. One of the interesting examples is from the non-transition metal chalcogenide's study: Cu-intercalated Bi<sub>2</sub>Se<sub>3</sub> nanoribbons. Bi<sub>2</sub>Se<sub>3</sub> nanoribbons are usually synthesized as n-doped semiconductors, showing silvery white color. But large amounts of intercalated Cu atoms, up to 60 atomic percent, turn the color of the nanoribbons to orange color, due to such high concentration of copper inside.<sup>67</sup> In addition, Cu intercalation into very thin 2D layers of Bi<sub>2</sub>Se<sub>3</sub> manifests an unexpected optical transition in visible light wavelengths.<sup>68</sup> Fig. 4(c) contains optical transmission

images of ultrathin Bi<sub>2</sub>Se<sub>3</sub> nanoplates before (top) and after (bottom) Cu intercalations, showing a dramatic change in optical transmittance of 2D materials *via* intercalation. The increasing transmittance of 2D materials is attributed to the increase of the effective bandgap due to the large free electron density introduced by metal atom intercalation. The concept of optical property tuning *via* intercalation can be generalized to the organic molecules. For example, a plasmonic peak shift by molecular intercalation has been demonstrated.<sup>69</sup> Such intercalation tuning methods of optical and plasmonic properties are expected to be applied to many TMD structures in similar passion.

### 3.2 Intercalation tuning of catalytic activity

In catalysis, scientists have revealed the strong correlation between the electronic structure and the catalytic activity through theoretical simulations as well as experimental demonstrations.<sup>12,45–49</sup> Proper electronic structures of the active atomic sites should be designed to create suitable chemical bonding with the reactants (not too weak and not too strong), which ensures both a good electron transfer between the catalysts and the reagents and a facile products-releasing process.<sup>12</sup> Therefore, the tunable electronic structure through electrochemical or chemical intercalation makes 2D TMD materials very attractive candidates for catalysis optimization. Electrochemical intercalation can effectively shift the chemical potentials of 2D TMD materials within a wide range, getting to the optimized position for efficient catalysis. Sometimes the intercalation process introduces a phase transition of the host matrix, significantly changing the electronic structure to another form which may perform excellent catalytic activity.<sup>70–74</sup> In addition, the intercalated guest atoms and the matrix material may have charge transfers between each other as

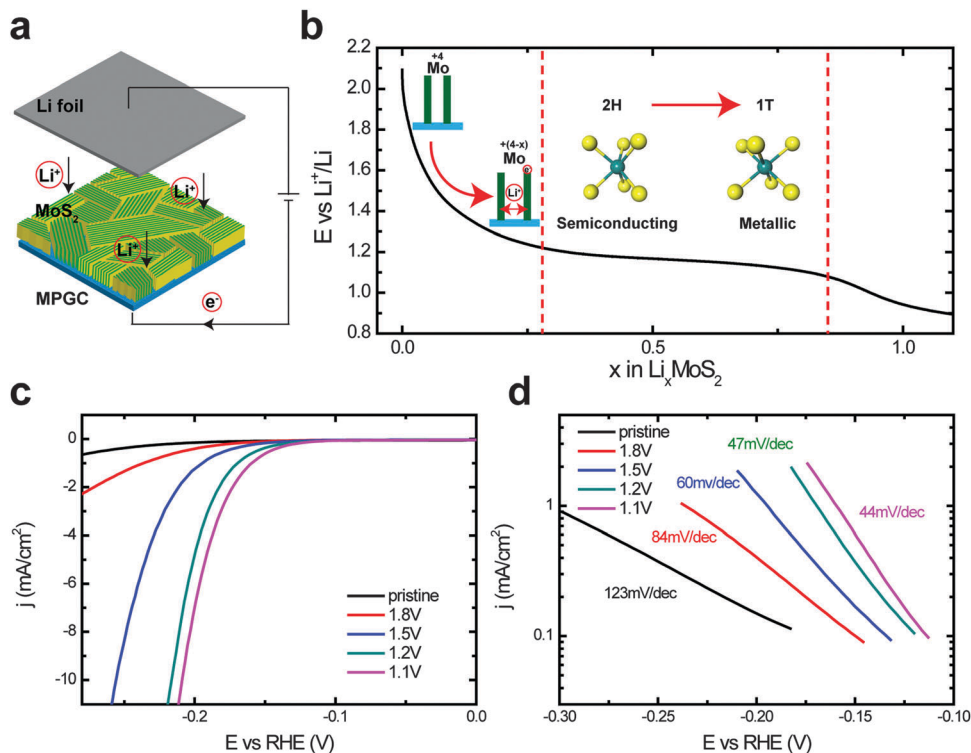


Fig. 5 (a) Schematic of the edge-terminated MoS<sub>2</sub> lithiation process. (b) Galvanostatic discharge curve with schematics of charge transfer and phase transition. (c) Improved HER performance after the Li tuning process. (d) The corresponding Tafel slopes of MoS<sub>2</sub> lithiated to different voltages. Reproduced with permission from ref. 71. Copyright 2013, National Academy of Sciences, USA.

illustrated in Fig. 1(c), which increases the carrier density and thus improves the conductivity of the catalyst.<sup>71</sup> A successful example is lithium electrochemical tuning of 2H MoS<sub>2</sub> for enhanced HER activity developed in our group.<sup>71,75</sup> As shown in Fig. 5(a), the as-synthesized edge-terminated MoS<sub>2</sub> nanofilm and a piece of Li foil were made into a pouch battery cell to perform Li intercalation.<sup>71</sup> A galvanostatic discharge curve is shown in Fig. 5(b), providing useful information regarding the MoS<sub>2</sub> electronic structure change such as the lowered Mo oxidation state and the MoS<sub>2</sub> 2H to 1T phase transition. The intercalated Li transfers excess charge carriers to MoS<sub>2</sub>, reducing the oxidation state of Mo, increasing the electronic energy of the whole system, and thus inducing the structure phase transition for a more stable octahedral coordination. This electronic structure change helps to improve the HER catalytic activity significantly as shown in Fig. 5(c). The chemical potential of Li intercalated MoS<sub>2</sub> was continuously shifted from the open circuit voltage to 1.1 V vs. Li<sup>+</sup>/Li and stopped at different intermediate voltages. Consequently, the HER performance is continuously improved, with the Tafel slopes improved from 123 mV per decade all the way to 44 mV per decade. It should be noted that the 1T phase MoS<sub>2</sub> is still stable even though the Li inside reacts with air and water.<sup>71,75,76</sup>

Another way to tune the electronic structure of MoS<sub>2</sub> and WS<sub>2</sub> nanosheets for improved HER activity is chemical intercalation.<sup>72,73,76,77</sup> Chhowalla and coworkers successfully prepared 1T phase WS<sub>2</sub> nanosheets by a chemical intercalation and exfoliation process.<sup>73</sup> The TEM images of 2H and 1T WS<sub>2</sub> single layers show the atomic structure change. 2H WS<sub>2</sub> shows the hexagonal lattice, which undergoes a phase transition to

form a distorted 1T structure with a  $2a_0 \times a_0$  superlattice. The HER performance of 2H WS<sub>2</sub> was significantly improved after the phase transition. The reason for this change was revealed by their theoretical simulation that showed the strains in the 1T nanosheets help to lower the reaction free energy.<sup>73</sup> Jin and his coworkers' study of 1T MoS<sub>2</sub> nanosheets obtained similar results.<sup>72</sup> The *n*-butyl lithium was utilized as the intercalation solution. This solution helps to chemically intercalate a large amount of Li atoms into the MoS<sub>2</sub>, shift the MoS<sub>2</sub> to low chemical potential, exfoliate the nanosheets into single or few layers, and induce the 2H to 1T phase transition.<sup>72</sup> The performance of the metallic 1T MoS<sub>2</sub> was tremendously improved from the semiconducting 2H phase, with a Tafel slope of 43 mV per decade. Several follow-up studies employed both electrochemical and chemical intercalation methods for further improved HER activities.<sup>75–77</sup> It should be mentioned that the electrochemical tuning method has also been demonstrated to be effective to enhance electrocatalysis of other forms of 2D materials such as lithium transition metal oxides.<sup>74</sup> Therefore, 2D TMD materials with the intercalation tuning properties constitute a vast screening pool of efficient catalysts.

## 4. Heterostructure and alloying tuning

### 4.1 Heterostructure tuning

As the leading 2D material, graphene is reported to achieve high electronic mobility exceeding  $100\,000\text{ cm}^2\text{ V}^{-1}\text{ s}^{-1}$  by

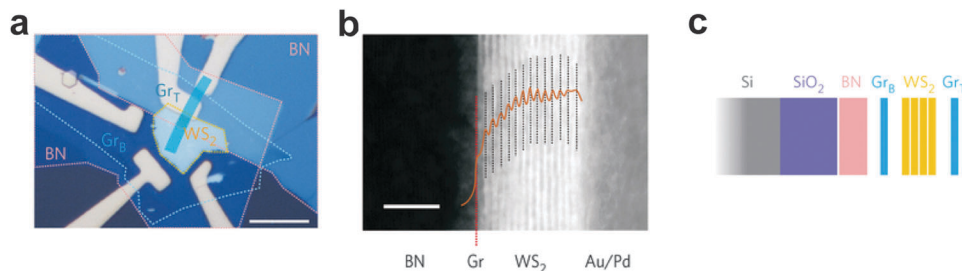


**Fig. 6** Graphene–WS<sub>2</sub> vertical heterostructure. (a) Optical microscopy image of the device (scale bar, 10 μm). (b) Cross-section high-resolution high-angle annular dark-field scanning transmission electron microscopy (HAADF STEM) image (scale bar, 5 nm). (c) Schematic of vertical architecture of the transistor. Reproduced with permission from ref. 79. Copyright 2013, Nature Publishing Group.

artificially stacking graphene on top of hBN to form a heterostructure.<sup>78</sup> This work first attracted attention to tuning the properties of 2D materials *via* forming heterostructures from materials with different bandgaps and work functions.<sup>6</sup> In addition, graphene/h-BN heterostructure also demonstrates more exotic physics, known as Hofstadter's butterfly. Similar to graphite, TMDs MX<sub>2</sub> crystallizes in a vertically stacked, weakly interacted layered structure. Hence, the individual monolayers can be mechanically exfoliated by the simple Scotch-tape technique,<sup>2</sup> which makes it easy to obtain building blocks for heterostructure assembly. Due to the sulfur/selenium terminated surface with no dangling bond, the heterostructures can have clean and atomically sharp interfaces as shown in Fig. 6(b).<sup>79</sup> The tunability of properties *via* assembling high-quality heterostructures, together with the impressive characterization of TMDs mentioned in previous sections, make TMDs promising candidates for band engineering<sup>80</sup> and functional heterostructure design.<sup>2,8,81–84</sup>

**Vertical heterostructure.** The first observation of such tunability is reported as field effect tunneling transistors<sup>79,85</sup> with multilayer MoS<sub>2</sub> or WS<sub>2</sub> serving as a vertical transport barrier on top of graphene as shown in Fig. 6(a). Both theoretical<sup>86</sup> and experimental results<sup>87</sup> show that partially ionized donors in MoS<sub>2</sub> transfer charge to the graphene to shift the Fermi level of graphene and lower the height of the tunnel barrier. Hence, with MoS<sub>2</sub> or WS<sub>2</sub> serving as barrier materials, the ON/OFF ratio of the FETT will increase, since the changes in the Fermi level of the graphene can be equal to or larger than the barrier height. For example, due to the advantage of switching between tunneling and thermionic transport regimes, transistors exceeding a 10<sup>6</sup> ON/OFF ratio are reported at room temperature in a graphene–WS<sub>2</sub> transistor.<sup>79</sup> The gate tunability in vertical heterostructures between TMDs and graphene allows devices with different functions be constructed such as nonvolatile memory cells,<sup>88–90</sup> complementary inverters,<sup>91</sup> photoresponsive memory devices.<sup>92</sup> Further, based on the enhancement on photon absorption and electron-hole creation due to the Van Hove singularities in the electronic density of states of TMDs,<sup>93</sup> flexible photovoltaic devices were also demonstrated.<sup>93,94</sup> Besides, heterostructures between TMDs and other 2D materials such as carbon nanotubes<sup>95</sup> and amorphous silicon<sup>96</sup> were also reported to tune the properties of TMDs.<sup>97</sup>

Another example of tuning band structure is the heterostructure formed by two different TMDs.<sup>98</sup> Researchers created

an atomically sharp, type II heterostructure with atomically thin layers of WSe<sub>2</sub> (p-type) and MoS<sub>2</sub> (n-type). This type of heterostructure introduces highly asymmetric charge transfer rates for electrons and holes, which drive the spontaneous dissociation of a photogenerated exciton into free carriers. It is reported that photoluminescence decreased dramatically in the p–n junction area. To further tune the device properties *via* forming heterostructures, researchers sandwiched the p–n junction with two graphene electrodes and obtained a five times increase in the photoresponsivity than typical laterally-contacted devices.

Besides simply forming vertical heterostructures, in recent studies, changing the interlayer twist angle has been demonstrated to tune material properties.<sup>99</sup> They reported that the energy for the valence band edge state at the  $\Gamma$  point is sensitive to interlayer interactions, while the energies at  $K$  point are relatively insensitive. Besides, owing to repulsion between sulfur atoms, the interlayer distance varies with different twists, providing a potential tool to tune the physical properties of 2D heterostructures, including indirect optical transition energy and second-harmonic generation effects.

In previous studies, the small size and low yield of manually stacking assemblies limited the industrial application of TMD heterostructure devices. A scalable approach to these heterostructures was reported in a recent work.<sup>100</sup> By selenization of MoO<sub>3</sub> *via* a chemical vapor deposition method, the authors demonstrated large-area monolayer MoSe<sub>2</sub>/graphene heterostructure, which might open up the industrial applications of heterostructures in optoelectronics, electronics and photocatalysis.

**Lateral heterostructures.** Beyond these great efforts made on vertical designed heterostructures, it is also possible to tune the material properties *via* forming p–n heterostructures in the lateral direction. The first trial of this design was demonstrated by forming lateral p–n homojunctions by using electrostatic doping. With this method three groups reported similar studies on the WSe<sub>2</sub> based lateral p–n junction, showing impressive optoelectronic properties *via* this lateral tuning.<sup>101–103</sup> However lateral heterostructures can only be achieved through direct growth between two different materials. As that happened in the development of vertical heterostructures, this design was first presented by a ‘patterned regrowth’ process between graphene and hBN to demonstrate atomically thin circuitry.<sup>104</sup>

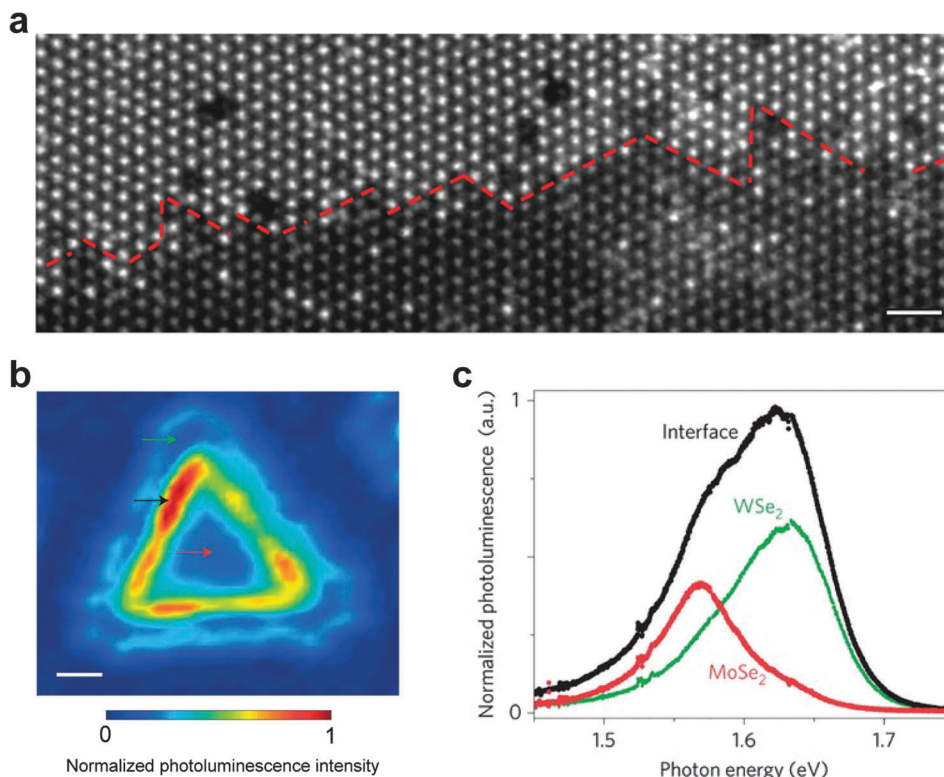


**Fig. 7** TMD lateral heterostructures. (a) Atomic-resolution Z-contrast STEM images of the in-plane interface between WS<sub>2</sub> and MoS<sub>2</sub> domains. The red dashed lines highlight the atomically sharp interface along the zigzag-edge direction. Scale bar, 1 nm. Reproduced with permission from ref. 107. Copyright 2014, Nature Publishing Group. (b) 2D Photoluminescence intensity map of lateral heterostructure. Intense emission is seen from the 1D interface. Scanning micro-photoluminescence was performed with 532 nm laser excitation at room temperature. Scale bars, 2  $\mu$ m. Reproduced with permission from ref. 105. Copyright 2014, Nature Publishing Group. (c) Photoluminescence spectra taken at the points indicated by the corresponding coloured arrows in (b). Reproduced with permission from ref. 105. Copyright 2014, Nature Publishing Group.

Recently, three groups reported successful synthesis of such lateral heterostructures in TMDs *via* atomic vapour pressure variation led sequential growth,<sup>105</sup> *in situ* reactant modulation,<sup>106</sup> and growth rate difference selected sequential growth<sup>107</sup> respectively. It is also shown that the precise reaction temperature can select the final structure between vertically stacked bilayers and in-plane lateral heterojunctions.<sup>107</sup> All three studies reported the observation of a seamless and atomically sharp interface as shown in Fig. 7a. EDS and Raman elemental mapping shows the existence of lateral heteroepitaxy growth between TMDs with high crystalline quality. Besides, strong localized photoluminescence enhancement is observed around the interface as shown in Fig. 7b and c. Based on the successful obtainment of such p-n heterostructures researchers demonstrated a CMOS inverter by integrating a p-type WSe<sub>2</sub> and an n-type WS<sub>2</sub> FET and reported a voltage gain as large as 24. As a new tuning method, more interesting properties are expected from TMD lateral heterostructures.

#### 4.2 Alloying tuning

Ternary two-dimensional dichalcogenide alloys exhibit compositionally modulated electronic structure, and hence, control of alloy concentration within each individual layer of these compounds provides a powerful tool to efficiently modify their physical and chemical properties, including the carrier effective

mass and bandgap.<sup>108–111</sup> As mentioned above, the electronic properties of TMDs are qualitatively determined by the localization behavior of the d-bands of the transition metal. Depending on the degree of localization, these materials can be insulators, semiconductors, semimetals, or metals. The degree of d-state mixing depends on the nature of the transition metal and its chalcogen ligand environment, and is expected to be influenced by its substitutions in an alloy.<sup>108</sup> By using alloys of two of these MX<sub>2</sub> materials (either metal elements or chalcogens) one could achieve an even greater flexibility and access an almost continuous range of properties. The ability to tune continuously the bandgap of this distinctive class of atomically thin materials through the growth of S/Se alloys opens up many new possibilities for basic studies and device concepts.

Theoretical band calculation can always give us the rational design on bandgap engineering. Fig. 8(a) gives us the guidance, in which the differences in theoretical bandgaps are plotted *versus* the mismatch of the lattice constants before the alloying of two layered MX<sub>2</sub> semiconductors.<sup>108</sup> The data points in the upper corner of Fig. 8(a) correspond to the largest difference in bandgaps and the smallest lattice mismatch. Generally, when mixing the electron-deficient V (also for group 5 metals, such as Nb, and Ta) with group 6 semiconductors such as CrX<sub>2</sub>, MoX<sub>2</sub>, or WX<sub>2</sub>, the decrease in the electron number leads to metallic

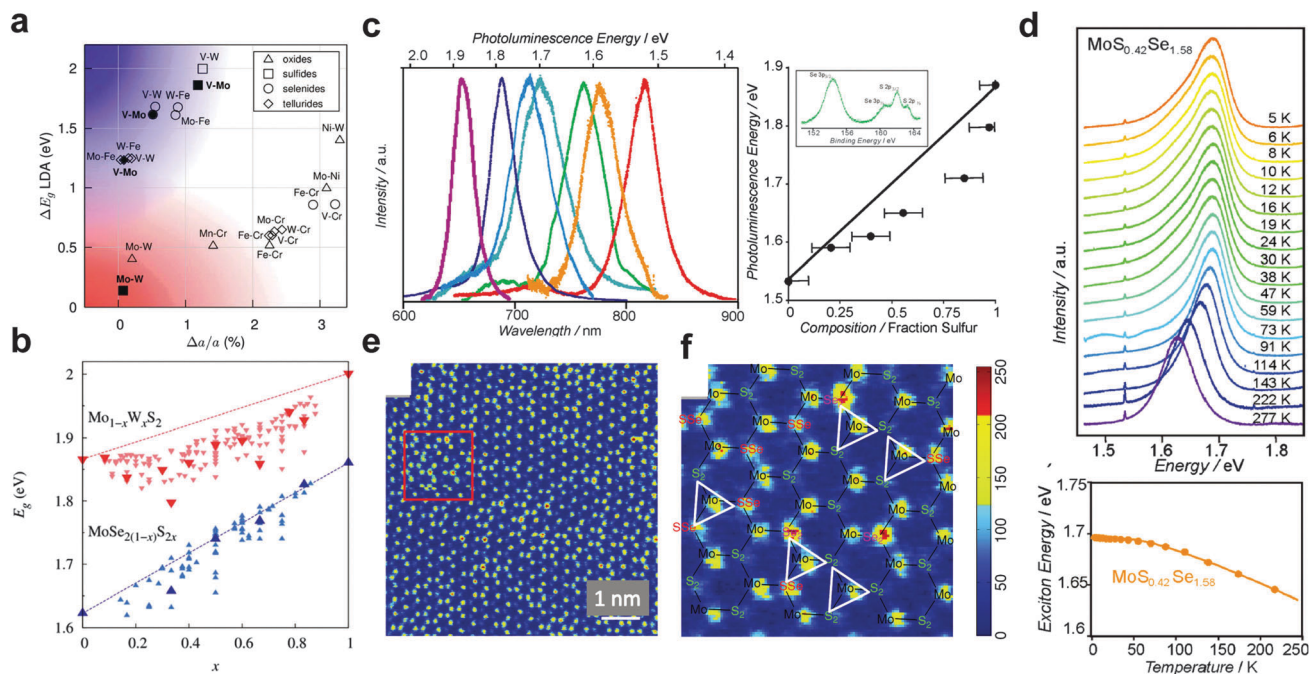


**Fig. 8** (a) Theoretical band gaps of binary alloys as a function of their lattice constants. Triangles designate oxides, squares – sulfides, circles – selenides, and diamonds – tellurides. Reproduced with permission from ref. 108. Copyright 2014, Royal Society of Chemistry. (b) LDA band gaps in  $\text{Mo}_{1-x}\text{W}_x\text{S}_2$  (downward triangles, red) and  $\text{MoSe}_2(1-x)\text{S}_{2x}$  (upward triangles, blue) alloys as a function of concentration  $x$ . The band gaps in the thermodynamic ground states are shown with larger symbols. Reproduced with permission from ref. 108. Copyright 2014, Royal Society of Chemistry. (c) Normalized RT PL spectra of  $\text{MoS}_2(1-x)\text{Se}_{2x}$  films of different composition. Right panel: variation of the photon energy of the PL emission peak as a function of sample composition, as determined by XPS (the inset shows a representative XPS spectrum of the Se-3p and S-2p peaks). The black line indicates a linear variation between the values of the stoichiometric compounds as found in DFT calculations. Reproduced with permission from ref. 109. Copyright 2013, John Wiley and Sons. (d) PL spectra for a  $\text{MoS}_{0.42}\text{Se}_{1.58}$  film at different temperatures between 277 and 5 K. All spectra are scaled to the same height. The bottom shows the exciton emission energy as a function of the temperature. Reproduced with permission from ref. 109. Copyright 2013, John Wiley and Sons. (e) HAADF-STEM image in false color. Mo sites: yellow;  $\text{S}_2$  sites: light blue;  $\text{SSe}$  sites: yellow, and  $\text{Se}_2$  sites: red. The red square in (e) outlines the part of the image shown in (f). The color scale shown in (d) is HAADF-STEM intensity in arbitrary units, in which different intensity ranges are shown in different colors. Reproduced with permission from ref. 114. Copyright 2014, John Wiley and Sons.

behavior and the shift of the Fermi level into the valence band. Mo–W dichalcogenide alloys are located at the bottom corner of the plot, indicating good lattice matching and moderate band-gap variation with concentration. The bandgaps in the thermodynamic ground states are shown with larger symbols. The LDA gap varies from 1.87 to 2.0 eV in  $\text{Mo}_{1-x}\text{W}_x\text{S}_2$  with concentration, close to the experimentally reported variation from 1.85 to 1.99 eV in this alloy.<sup>112,113</sup>

Unlike alloying by mixing metals, chalcogen alloys generally have a more limited range of possible variations in the bandgap than in the case of a mixing metal alloy. The synthesis of molybdenum disulfide, substitutionally doped with a broad range of selenium concentrations, results in optical bandgap modulations in atomic layers. Based on the CVD grown monolayer films, the photoluminescence and Raman measurements show that the band structure of the alloy films can be tuned continuously with composition. Both the experimental and theoretical studies show that the material exhibits a direct gap for all alloy compositions. The room temperature optical bandgap changes smoothly between the limits of 1.87 eV (for pure single-layer  $\text{MoS}_2$ ) and 1.55 eV (for pure single-layer  $\text{MoSe}_2$ ). Similarly, based on a one-step direct synthesis of  $\text{MoS}_2(1-x)\text{Se}_{2x}$

atomic mono- and bilayers with tunable compositions through CVD controlled selenium doping, the band structure of  $\text{MoS}_2$  could be modified and the optical bandgap could be continuously tuned by over 200 meV. Using atomic resolution Z-contrast imaging, direct atomic identification of Se dopants within the  $\text{MoS}_2$  lattice with almost 100% detection efficiency was demonstrated.<sup>114</sup>

In order to better understand and fine-tune the desired properties by alloying, quantifying and locating the alloy atoms within each layer is of great importance. The statistics of the homo- and hetero-atomic coordinates in single-layered  $\text{Mo}_{1-x}\text{W}_x\text{S}_2$  was obtained from the atomically resolved scanning transmission electron microscope images. These images successfully quantify the degree of alloying for the transition metal elements (Mo or W).<sup>110,115</sup> The direct visualization of the atomic species Mo and W in  $\text{Mo}_{1-x}\text{W}_x\text{S}_2$  compounds *via* chemical analysis using Z-contrast imaging with scanning transmission electron microscope (STEM) annular dark-field (ADF) clearly shows how the two elements can be mixed in a single layer. Also, it was used to count the neighboring atoms of two transition metal components that show either mutual attraction or repulsion of the constituent species. The random alloying of such a mixed dichalcogenide system throughout the chemical compositions

provides a direct proof of the alloying degree on individual atomic basis.

## 5. Gating, pressure, and lighting tuning

### 5.1 Electric field gating effect

Electric-field control of charge carrier density has attracted much attention since it is remarkably simple for modulating physical properties of condensed matters and for exploring new functionalities with a transistor configuration.<sup>8,116,117</sup> Adding carriers to layered chalcogenides can produce remarkable collective electronic effects owing to their enriched electronic phases, such as charge density wave and superconductivity.<sup>19</sup> Besides the chemical doping/intercalation mentioned above, electric-field tuning of surface carrier density through carrier accumulation or depletion in TMD-based field-effect-transistors is free from additional structural disorder and operating in a controllable/reversible way, especially at their monolayer limit. Therefore, to control electronic phases of layered TMDs in electrical means is attracting growing interest not only for understanding the fundamental physics but also practical electronics and spintronics applications.<sup>118</sup>

The 2D nature of the layered TMDs and the resulting carrier quantum confinement<sup>38</sup> decides that the layered TMDs can serve as the ideal charge transport channel for a high performance transistor. As an example, the field effect transistors based on a single layer MoS<sub>2</sub> with oxide as a gate insulator exhibit a large current on/off ratio exceeding  $1 \times 10^8$  at room temperature<sup>8,119,120</sup> which serve as the platform towards the realization of electronics and low-standby-power integrated circuits based on two-dimensional materials. The presence of the quantum mechanical confinement and further modification of the interfacial band alignment with the external gate electric field<sup>121</sup> provide us with the room-temperature field effect transistors with a very large on/off ratio and thus allow the observation of a metal–insulator transition in monolayer MoS<sub>2</sub>.<sup>116</sup> It should be addressed that the 2D nature of the TMDs results in charge transport that is highly sensitive to a number of factors such as substrates/dielectric,<sup>122–125</sup> cleanliness (surface adsorbates),<sup>126–132</sup> and contact metals,<sup>133–139</sup> providing the possibilities of the mobility enhancement/engineering with these factors.

To realize novel field-effect modulated electronic phenomena in solids, a broad range of attainable carrier density is always required. The power of an electric double layer transistor with ionic liquid gating to achieve high sheet carrier densities beyond the maximum attainable range of conventional oxide gate dielectrics has been recently exploited to modulate novel electronic properties and quantum phenomena on chalcogenides.<sup>140–142</sup> The access of field-effect induced emergent phenomena such as superconductivity, ferromagnetism and metal–insulator transitions with EDLTs provides a powerful way to study novel physical phenomena at such highly-charged interfaces.<sup>141–144</sup> The recent application of the ionic gating technique allows the achievement of the ultrathin carrier

density on MX<sub>2</sub> surfaces and large regime tuning of the Fermi level in the band structure. This powerful technique further plays a vital role in the experimental realization of the electric field induced Zeeman polarization,<sup>23</sup> the ambipolar operated transistor,<sup>145–148</sup> and the gating induced superconductivity in MX<sub>2</sub> systems (Fig. 9a–c).<sup>149,150</sup>

As another advantage of the transistor configuration, the intrinsic inversion symmetry can be broken simply by applying a perpendicular electric field in bilayer or bulk two-dimensional electron systems where the crystal symmetry governs the nature of electronic Bloch states.<sup>145,151</sup> For example, in bilayer MoS<sub>2</sub> transistors, the circularly polarized photoluminescence can be continuously tuned from –15 to 15% as a function of gate voltage, whereas in the structurally non-centrosymmetric monolayer MoS<sub>2</sub> case the photoluminescence polarization is gate independent.<sup>151</sup> The observations demonstrated the continuous tuning of orbital magnetic moments between positive and negative values through symmetry control by an electric field. More interestingly, with the electric field induced inversion symmetry breaking, a spin-coupled valley photocurrent whose direction and magnitude depend on the degree of circular polarization of the incident radiation can be further greatly modulated with an external electric field in an electric-double-layer transistor based on WSe<sub>2</sub>.<sup>152</sup> Such room temperature generation and electric control of valley/spin photocurrent provide a new property of electrons in MX<sub>2</sub> systems, thereby enabling new degrees of control for quantum-confined spintronics devices.<sup>152–154</sup>

### 5.2 Pressure induced insulator–metal transition

Unlike mono-atomic multilayered graphene with sp<sup>2</sup> hybridization, multilayered MoS<sub>2</sub> coupled with its d-orbital electronic states and small vdW gap raises the prospects of strong S–S interlayer interactions under axial compression that might lead to an electronic phase transition (Fig. 9d).<sup>155</sup> With high pressure experiments on exfoliated single crystalline MoS<sub>2</sub> up to 35 GPa, it was found that the pressure induced a lattice distortion involving anisotropic *c/a* axial compression beginning at ~10 GPa in multilayered MoS<sub>2</sub>. This compression leads to an intermediate state followed by a pressure-induced insulator–metal transition at ~19 GPa. First-principle theoretical calculations attribute the origin of the metallic electronic states to S–S interactions as the vdW gap closes at high pressures. The pressure control provides a possibility for the development of nanoscale pressure switches, sensors and multi-physics devices with coupled electrical, vibrational, optical and structural properties using multilayered MoS<sub>2</sub> and semiconducting TMDs.<sup>155</sup>

### 5.3 Valley polarization by circularly-polarized light

From the physics viewpoint, the recent emergence of transition metal dichalcogenides provides a new platform for exploring the internal quantum degrees of freedom of electrons including the electron spin, the layer pseudospin, and the valley pseudospin.<sup>156</sup> Owing to hexagonal in-plane lattice structure, where valleys of energy-momentum dispersion are generally expected at the corners of the hexagonal Brillouin zone (at the *K* and  $-K$  points), new

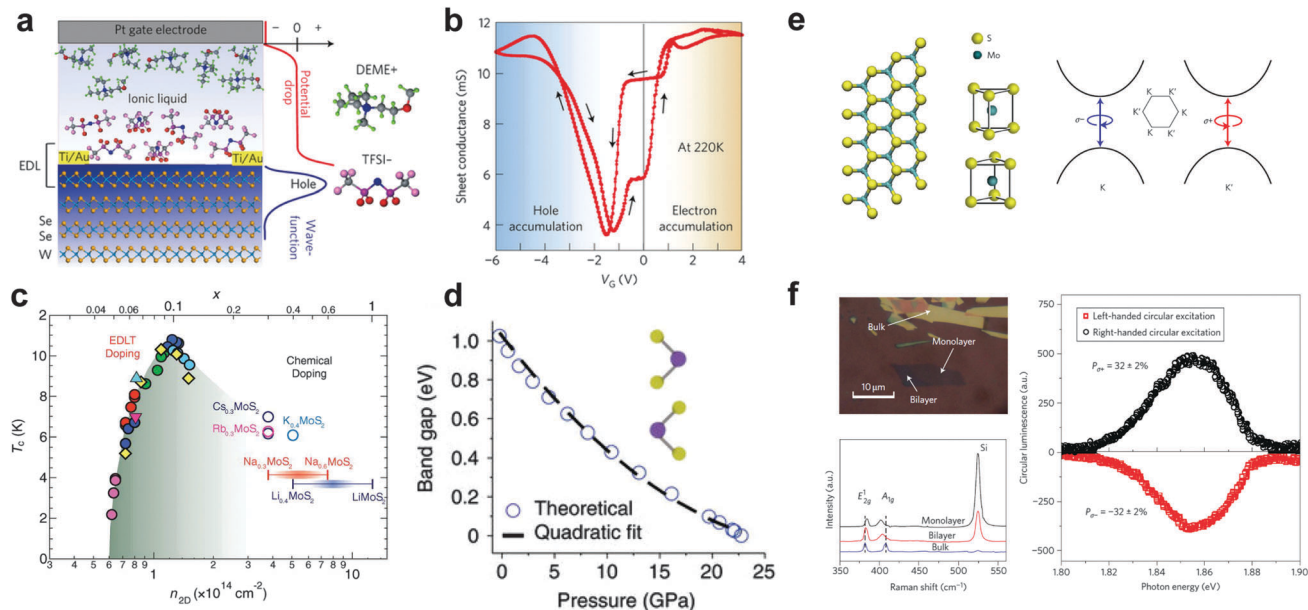


**Fig. 9** (a) Schematic structure of a typical WSe<sub>2</sub> EDLT. By applying a negative  $V_G$  through a Pt gate electrode, anions in the ionic liquid are electrostatically driven to the WSe<sub>2</sub> surface, forming a highly charged electric double layer (EDL) interface. Most of potential drop occurs at the EDL interface and almost no potential is distributed in the liquid. Reproduced with permission from ref. 145. Copyright 2013, Nature Publishing Group. (b) Ambipolar operation in the transfer characteristics of WSe<sub>2</sub> EDLTs. Reproduced with permission from ref. 145. Copyright 2013, Nature Publishing Group. (c) Unified phase diagram of superconductivity of both electrostatically and chemically doped MoS<sub>2</sub> as a function of doping concentration  $x$  (upper horizontal axis) and carrier density  $n_{2D}$  (bottom horizontal axis). The field-induced superconducting data were from four different samples, each marked with a differently shaped filled symbol. Filled circles of the same color correspond to the superconducting states at a fixed  $V_{LG}$  but different  $V_{BG}$ 's. Open circles show  $T_c$  of MoS<sub>2</sub> chemically intercalated with different alkali metal dopants. Solid bars denote the range of doping showing the same  $T_c$ . The structure of all intercalated compounds is 2H-type within the indicated carrier density region. Reproduced with permission from ref. 150. Copyright 2012, the American Association for the Advancement of Science. (d) Theoretical calculation of the pressure-dependent band gap of multilayered MoS<sub>2</sub>. The bandgap–pressure dependence can be modeled as a quadratic function,  $E_g = E_{g0} + aP + bP^2$  was used, where  $a = -70$  meV GPa<sup>-1</sup> and  $b = 1.13$  meV GPa<sup>-2</sup>. Reproduced with permission from ref. 155. Copyright 2014, Nature Publishing Group. (e) Schematic of the MoS<sub>2</sub> monolayer and optical selection rules at the  $K$  ( $K'$ ) point. Left panel: schematic of the MoS<sub>2</sub> monolayer structure with the spatial inversion symmetry breaking in monolayers. Right panel, Schematic of proposed valley-dependent selection rules at  $K$  and  $K'$  points in crystal momentum space: left (right)-handed circularly polarized light  $\sigma+$  ( $\sigma-$ ) only couples to the band-edge transition at  $K$  ( $K'$ ) points for the sake of angular momentum conservation and time reversal symmetry. Reproduced with permission from ref. 25. Copyright 2012, Nature Publishing Group. (f) Polarization-sensitive photoluminescence spectra from MoS<sub>2</sub> monolayers. Up-left: representative optical image of the MoS<sub>2</sub> monolayer, bilayer and thin film flakes. Down-left: characteristic Raman spectra from different MoS<sub>2</sub> flakes (monolayer, bilayer and thin film). Right panel: polarization resolved luminescence spectra under circularly polarized excitation from a He–Ne laser at 1.96 eV and 10 K. Reproduced with permission from ref. 25. Copyright 2012, Nature Publishing Group.

methods for the quantum control of the spin and these pseudospins arise from the existence of Berry phase-related physical properties and strong spin–orbit coupling.<sup>157</sup> Following theoretical discoveries of the intrinsic physical properties associated with valley pseudospin, experimental progress has been made in the control and tuning of valley polarization and coherence that allows manipulation in ways similar to real spin. Valley polarization, as the selective population of one valley is designated, has been demonstrated in monolayer MoS<sub>2</sub> by optical pumping with circularly polarized light (Fig. 9e and f).<sup>23–25</sup>

Several groups have independently reported the selective photoexcitation of the degenerate valleys by circularly polarized optical pumping in MoS<sub>2</sub> monolayers. The inversion symmetry present in bulk and in thin films with an even number of layers is explicitly broken in thin films with an odd number of layers, giving rise to a valley-contrasting optical selection rule,<sup>158,159</sup> where the inter-band transitions in the vicinity of the  $K$  ( $K'$ ) point couple exclusively to right (left)-handed circularly polarized light

$\sigma+$  ( $\sigma-$ ).<sup>23–25</sup> The direct-bandgap transition at the two degenerate valleys, together with this valley-contrasting selection rule, suggests that one can optically generate and detect valley polarizations in a MoS<sub>2</sub> monolayer.

## 6. Conclusions and outlook

In conclusion, we present different physical and chemical strategies, including reducing dimension along  $z$  and  $xy$  directions, intercalation of guest ions, stacking heterostructures, alloying different transition metals or chalcogens, electrical field effects, high pressure, and lighting, for the property tuning of 2D TMDs. The tuning methods and corresponding tunable properties are summarized in Table 1. The tunability of these layered materials leads to not only fundamental studies of material properties but also versatile applications in different areas. However, there is still much room for the development of

Table 1 Summary of 2D TMD tuning strategies and tunable properties

Tuning strategies	Tunable properties
z direction dimension	Electronic band structure, optical property
xy directions dimension	Electronic band structure, catalytic activity
Intercalation	Thermal conductivity, super conductivity, optical property, catalytic activity
Heterostructure	Electronic and optical properties
Alloying	Bandgap, carrier density and effective mass, optical property
Gating	Carrier density and mobility, optical property
Pressure	Electronic property
Lighting	Valley polarization

tunable 2D TMDs. For example, the synthesis of large scale and high quality single layer 2D TMDs needs to be further boosted for high performance devices; band structure and Fermi level tuning may become powerful tools in photoelectrocatalysis; carrier density tuning has the potential for optimizing the superconducting temperature. A number of important and exciting studies and applications employing the tunable properties of 2D TMDs will certainly come out in the near future.

## Acknowledgements

We acknowledge support by the Department of Energy, Office of Basic Energy Sciences, Materials Sciences and Engineering Division, under Contract DE-AC02-76-SFO0515.

## References

- 1 K. S. Novoselov, A. K. Geim, S. V. Morozov, D. Jiang, Y. Zhang, S. V. Dubonos, I. V. Grigorieva and A. A. Firsov, *Science*, 2004, **306**, 666–669.
- 2 K. S. Novoselov, D. Jiang, F. Schedin, T. J. Booth, V. V. Khotkevich, S. V. Morozov and A. K. Geim, *Proc. Natl. Acad. Sci. U. S. A.*, 2005, **102**, 10451–10453.
- 3 A. K. Geim and K. S. Novoselov, *Nat. Mater.*, 2007, **6**, 183–191.
- 4 M. Xu, T. Liang, M. Shi and H. Chen, *Chem. Rev.*, 2013, **113**, 3766–3798.
- 5 L. Ci, L. Song, C. Jin, D. Jariwala, D. Wu, Y. Li, A. Srivastava, Z. F. Wang, K. Storr, L. Balicas, F. Liu and P. M. Ajayan, *Nat. Mater.*, 2010, **9**, 430–435.
- 6 Q. H. Wang, K. Kalantar-Zadeh, A. Kis, J. N. Coleman and M. S. Strano, *Nat. Nano*, 2012, **7**, 699–712.
- 7 S. Z. Butler, S. M. Hollen, L. Cao, Y. Cui, J. A. Gupta, H. R. Gutiérrez, T. F. Heinz, S. S. Hong, J. Huang, A. F. Ismach, E. Johnston-Halperin, M. Kuno, V. V. Plashnitsa, R. D. Robinson, R. S. Ruoff, S. Salahuddin, J. Shan, L. Shi, M. G. Spencer, M. Terrones, W. Windl and J. E. Goldberger, *ACS Nano*, 2013, **7**, 2898–2926.
- 8 B. Radisavljevic, A. Radenovic, J. Brivio, V. Giacometti and A. Kis, *Nat. Nano*, 2011, **6**, 147–150.
- 9 H. Zhang, C.-X. Liu, X.-L. Qi, X. Dai, Z. Fang and S.-C. Zhang, *Nat. Phys.*, 2009, **5**, 438–442.
- 10 Y. L. Chen, J. G. Analytis, J.-H. Chu, Z. K. Liu, S.-K. Mo, X. L. Qi, H. J. Zhang, D. H. Lu, X. Dai, Z. Fang, S. C. Zhang, I. R. Fisher, Z. Hussain and Z.-X. Shen, *Science*, 2009, **325**, 178–181.
- 11 M. Chhowalla, H. S. Shin, G. Eda, L.-J. Li, K. P. Loh and H. Zhang, *Nat. Chem.*, 2013, **5**, 263–275.
- 12 B. Hinnemann, P. G. Moses, J. Bonde, K. P. Jørgensen, J. H. Nielsen, S. Horch, I. Chorkendorff and J. K. Nørskov, *J. Am. Chem. Soc.*, 2005, **127**, 5308–5309.
- 13 H. Li, J. Wu, Z. Yin and H. Zhang, *Acc. Chem. Res.*, 2014, **47**, 1067–1075.
- 14 X. Huang, C. Tan, Z. Yin and H. Zhang, *Adv. Mater.*, 2014, **26**, 2185–2204.
- 15 X. Huang, Z. Zeng and H. Zhang, *Chem. Soc. Rev.*, 2013, **42**, 1934–1946.
- 16 D. Jariwala, V. K. Sangwan, L. J. Lauhon, T. J. Marks and M. C. Hersam, *ACS Nano*, 2014, **8**, 1102–1120.
- 17 D. Kong, H. Wang, J. J. Cha, M. Pasta, K. J. Koski, J. Yao and Y. Cui, *Nano Lett.*, 2013, **13**, 1341–1347.
- 18 M. S. Dresselhaus, *Intercalation in layered materials*, Plenum Press, New York, 1986.
- 19 J. A. Wilson and A. D. Yoffe, *Adv. Phys.*, 1969, **18**, 193–335.
- 20 L. Mattheiss, *Phys. Rev. B: Condens. Matter Mater. Phys.*, 1973, **8**, 3719.
- 21 A. C. Neto, *Phys. Rev. Lett.*, 2001, **86**, 4382.
- 22 Z. Yin, H. Li, H. Li, L. Jiang, Y. Shi, Y. Sun, G. Lu, Q. Zhang, X. Chen and H. Zhang, *ACS Nano*, 2012, **6**, 74–80.
- 23 T. Cao, G. Wang, W. P. Han, H. Q. Ye, C. R. Zhu, J. R. Shi, Q. Niu, P. H. Tan, E. Wang, B. L. Liu and J. Feng, *Nat. Commun.*, 2012, **3**, 887.
- 24 K. F. Mak, K. He, J. Shan and T. F. Heinz, *Nat. Nano*, 2012, **7**, 494–498.
- 25 H. Zeng, J. Dai, W. Yao, D. Xiao and X. Cui, *Nat. Nano*, 2012, **7**, 490–493.
- 26 H. J. Conley, B. Wang, J. I. Ziegler, R. F. Haglund, S. T. Pantelides and K. I. Bolotin, *Nano Lett.*, 2013, **13**, 3626–3630.
- 27 K.-K. Liu, W. Zhang, Y.-H. Lee, Y.-C. Lin, M.-T. Chang, C.-Y. Su, C.-S. Chang, H. Li, Y. Shi and H. Zhang, *Nano Lett.*, 2012, **12**, 1538–1544.
- 28 H. S. Lee, S.-W. Min, Y.-G. Chang, M. K. Park, T. Nam, H. Kim, J. H. Kim, S. Ryu and S. Im, *Nano Lett.*, 2012, **12**, 3695–3700.
- 29 Y. Shi, W. Zhou, A.-Y. Lu, W. Fang, Y.-H. Lee, A. L. Hsu, S. M. Kim, K. K. Kim, H. Y. Yang and L.-J. Li, *Nano Lett.*, 2012, **12**, 2784–2791.
- 30 Y. Zhan, Z. Liu, S. Najmaei, P. M. Ajayan and J. Lou, *Small*, 2012, **8**, 966–971.
- 31 Y.-H. Lee, X.-Q. Zhang, W. Zhang, M.-T. Chang, C.-T. Lin, K.-D. Chang, Y.-C. Yu, J. T.-W. Wang, C.-S. Chang, L.-J. Li and T.-W. Lin, *Adv. Mater.*, 2012, **24**, 2320–2325.
- 32 W. Zhu, T. Low, Y.-H. Lee, H. Wang, D. B. Farmer, J. Kong, F. Xia and P. Avouris, *Nat. Commun.*, 2014, **5**, 3087.
- 33 J. Wu, H. Schmidt, K. K. Amara, X. Xu, G. Eda and B. Özyilmaz, *Nano Lett.*, 2014, **14**, 2730–2734.
- 34 P. Joensen, R. F. Frindt and S. R. Morrison, *Mater. Res. Bull.*, 1986, **21**, 457–461.
- 35 Z. Zeng, Z. Yin, X. Huang, H. Li, Q. He, G. Lu, F. Boey and H. Zhang, *Angew. Chem., Int. Ed.*, 2011, **50**, 11093–11097.

- 36 T. S. Li and G. L. Galli, *J. Phys. Chem. C*, 2007, **111**, 16192–16196.
- 37 S. Lebegue and O. Eriksson, *Phys. Rev. B: Condens. Matter Mater. Phys.*, 2009, **79**, 115409.
- 38 A. Splendiani, L. Sun, Y. Zhang, T. Li, J. Kim, C.-Y. Chim, G. Galli and F. Wang, *Nano Lett.*, 2010, **10**, 1271–1275.
- 39 K. F. Mak, C. Lee, J. Hone, J. Shan and T. F. Heinz, *Phys. Rev. Lett.*, 2010, **105**, 136805.
- 40 W. C. Jin, P. C. Yeh, N. Zaki, D. T. Zhang, J. T. Sadowski, A. Al-Mahboob, A. M. van der Zande, D. A. Chenet, J. I. Dadap, I. P. Herman, P. Sutter, J. Hone and R. M. Osgood, *Phys. Rev. Lett.*, 2013, **111**, 106801.
- 41 Y. Zhang, T. R. Chang, B. Zhou, Y. T. Cui, H. Yan, Z. K. Liu, F. Schmitt, J. Lee, R. Moore, Y. L. Chen, H. Lin, H. T. Jeng, S. K. Mo, Z. Hussain, A. Bansil and Z. X. Shen, *Nat. Nanotechnol.*, 2014, **9**, 111–115.
- 42 R. Tenne, L. Margulis, M. Genut and G. Hodes, *Nature*, 1992, **360**, 444–446.
- 43 Y. Feldman, E. Wasserman, D. J. Srolovitz and R. Tenne, *Science*, 1995, **267**, 222–225.
- 44 R. Tenne, *Nat. Nano*, 2006, **1**, 103–111.
- 45 M. V. Bollinger, J. V. Lauritsen, K. W. Jacobsen, J. K. Nørskov, S. Helveg and F. Besenbacher, *Phys. Rev. Lett.*, 2001, **87**, 196803.
- 46 J. V. Lauritsen, J. Kibsgaard, S. Helveg, H. Topsoe, B. S. Clausen, E. Laegsgaard and F. Besenbacher, *Nat. Nano*, 2007, **2**, 53–58.
- 47 T. F. Jaramillo, K. P. Jørgensen, J. Bonde, J. H. Nielsen, S. Horch and I. Chorkendorff, *Science*, 2007, **317**, 100–102.
- 48 X. Huang, Z. Zeng, S. Bao, M. Wang, X. Qi, Z. Fan and H. Zhang, *Nat. Commun.*, 2013, **4**, 1444.
- 49 Z. Zeng, C. Tan, X. Huang, S. Bao and H. Zhang, *Energy Environ. Sci.*, 2014, **7**, 797–803.
- 50 C. Tsai, K. Chan, F. Abild-Pedersen and J. K. Nørskov, *Phys. Chem. Chem. Phys.*, 2014, **16**, 13156–13164.
- 51 H. Wang, D. Kong, P. Johanes, J. J. Cha, G. Zheng, K. Yan, N. Liu and Y. Cui, *Nano Lett.*, 2013, **13**, 3426–3433.
- 52 J. Bonde, P. G. Moses, T. F. Jaramillo, J. K. Nørskov and I. Chorkendorff, *Faraday Discuss.*, 2009, **140**, 219–231.
- 53 Y. Li, H. Wang, L. Xie, Y. Liang, G. Hong and H. Dai, *J. Am. Chem. Soc.*, 2011, **133**, 7296–7299.
- 54 Z. Chen, D. Cummins, B. N. Reinecke, E. Clark, M. K. Sunkara and T. F. Jaramillo, *Nano Lett.*, 2011, **11**, 4168–4175.
- 55 J. Kibsgaard, Z. Chen, B. N. Reinecke and T. F. Jaramillo, *Nat. Mater.*, 2012, **11**, 963–969.
- 56 J. Xie, H. Zhang, S. Li, R. Wang, X. Sun, M. Zhou, J. Zhou, X. W. Lou and Y. Xie, *Adv. Mater.*, 2013, **25**, 5807–5813.
- 57 H. I. Karunadasa, E. Montalvo, Y. Sun, M. Majda, J. R. Long and C. J. Chang, *Science*, 2012, **335**, 698–702.
- 58 F. R. Gamble, J. H. Osiecki, M. Cais, R. Pisharody, F. J. DiSalvo and T. H. Geballe, *Science*, 1971, **174**, 493–497.
- 59 D.-Y. Chung, T. Hogan, P. Brazis, M. Rocci-Lane, C. Kannewurf, M. Bastea, C. Uher and M. G. Kanatzidis, *Science*, 2000, **287**, 1024–1027.
- 60 C. Wan, Y. Wang, N. Wang, W. Norimatsu, M. Kusunoki and K. Koumoto, *J. Electron. Mater.*, 2011, **40**, 1271–1280.
- 61 J. Cho, M. D. Losego, H. G. Zhang, H. Kim, J. Zuo, I. Petrov, D. G. Cahill and P. V. Braun, *Nat. Commun.*, 2014, **5**, 4035.
- 62 E. Morosan, H. W. Zandbergen, B. S. Dennis, J. W. G. Bos, Y. Onose, T. Klimczuk, A. P. Ramirez, N. P. Ong and R. J. Cava, *Nat. Phys.*, 2006, **2**, 544–550.
- 63 Y. S. Hor, A. J. Williams, J. G. Checkelsky, P. Roushan, J. Seo, Q. Xu, H. W. Zandbergen, A. Yazdani, N. P. Ong and R. J. Cava, *Phys. Rev. Lett.*, 2010, **104**, 057001.
- 64 M. Kriener, K. Segawa, Z. Ren, S. Sasaki, S. Wada, S. Kuwabata and Y. Ando, *Phys. Rev. B: Condens. Matter Mater. Phys.*, 2011, **84**, 054513.
- 65 J. Guo, S. Jin, G. Wang, S. Wang, K. Zhu, T. Zhou, M. He and X. Chen, *Phys. Rev. B: Condens. Matter Mater. Phys.*, 2010, **82**, 180520.
- 66 M. Burrard-Lucas, D. G. Free, S. J. Sedlmaier, J. D. Wright, S. J. Cassidy, Y. Hara, A. J. Corkett, T. Lancaster, P. J. Baker, S. J. Blundell and S. J. Clarke, *Nat. Mater.*, 2013, **12**, 15–19.
- 67 K. J. Koski, J. J. Cha, B. W. Reed, C. D. Wessells, D. Kong and Y. Cui, *J. Am. Chem. Soc.*, 2012, **134**, 7584–7587.
- 68 J. Yao, K. J. Koski, W. Luo, J. J. Cha, L. Hu, D. Kong, V. K. Narasimhan, K. Huo and Y. Cui, *Nat. Commun.*, 2014, **5**, 5670.
- 69 J. J. Cha, K. J. Koski, K. C. Y. Huang, K. X. Wang, W. Luo, D. Kong, Z. Yu, S. Fan, M. L. Brongersma and Y. Cui, *Nano Lett.*, 2013, **13**, 5913–5918.
- 70 M. A. Py and R. R. Haering, *Can. J. Phys.*, 1983, **61**, 76–84.
- 71 H. Wang, Z. Lu, S. Xu, D. Kong, J. J. Cha, G. Zheng, P.-C. Hsu, K. Yan, D. Bradshaw, F. B. Prinz and Y. Cui, *Proc. Natl. Acad. Sci. U. S. A.*, 2013, **110**, 19701–19706.
- 72 M. A. Lukowski, A. S. Daniel, F. Meng, A. Forticaux, L. Li and S. Jin, *J. Am. Chem. Soc.*, 2013, **135**, 10274–10277.
- 73 D. Voiry, H. Yamaguchi, J. Li, R. Silva, D. C. B. Alves, T. Fujita, M. Chen, T. Asefa, V. B. Shenoy, G. Eda and M. Chhowalla, *Nat. Mater.*, 2013, **12**, 850–855.
- 74 Z. Lu, H. Wang, D. Kong, K. Yan, P.-C. Hsu, G. Zheng, H. Yao, Z. Liang, X. Sun and Y. Cui, *Nat. Commun.*, 2014, **5**, 4345.
- 75 H. Wang, Z. Lu, D. Kong, J. Sun, T. M. Hymel and Y. Cui, *ACS Nano*, 2014, **8**, 4940–4947.
- 76 D. Voiry, M. Salehi, R. Silva, T. Fujita, M. Chen, T. Asefa, V. B. Shenoy, G. Eda and M. Chhowalla, *Nano Lett.*, 2013, **13**, 6222–6227.
- 77 M. A. Lukowski, A. S. Daniel, C. R. English, F. Meng, A. Forticaux, R. J. Hamers and S. Jin, *Energy Environ. Sci.*, 2014, **7**, 2608.
- 78 C. Dean, A. Young, I. Meric, C. Lee, L. Wang, S. Sorgenfrei, K. Watanabe, T. Taniguchi, P. Kim and K. Shepard, *Nat. Nanotechnol.*, 2010, **5**, 722–726.
- 79 T. Georgiou, R. Jalil, B. D. Belle, L. Britnell, R. V. Gorbachev, S. V. Morozov, Y.-J. Kim, A. Gholinia, S. J. Haigh and O. Makarovsky, *Nat. Nanotechnol.*, 2013, **8**, 100–103.
- 80 J. Kang, S. Tongay, J. Zhou, J. Li and J. Wu, *Appl. Phys. Lett.*, 2013, **102**, 012111.
- 81 R. Cheng, D. Li, H. Zhou, C. Wang, A. Yin, S. Jiang, Y. Liu, Y. Chen, Y. Huang and X. Duan, arXiv preprint arXiv:1403.3447, 2014.
- 82 M. M. Furchi, A. Pospischil, F. Libisch, J. Burgdörfer and T. Mueller, *Nano Lett.*, 2014, **14**, 4785–4791.

- 83 K. Kořmider and J. Fernandez-Rossier, *Phys. Rev. B: Condens. Matter Mater. Phys.*, 2013, **87**, 075451.
- 84 X. Hong, J. Kim, S.-F. Shi, Y. Zhang, C. Jin, Y. Sun, S. Tongay, J. Wu, Y. Zhang and F. Wang, *Nat. Nano*, 2014, **9**, 682–686.
- 85 L. Britnell, R. Gorbachev, R. Jalil, B. Belle, F. Schedin, A. Mishchenko, T. Georgiou, M. Katsnelson, L. Eaves and S. Morozov, *Science*, 2012, **335**, 947–950.
- 86 B. Sachs, L. Britnell, T. Wehling, A. Eckmann, R. Jalil, B. Belle, A. Lichtenstein, M. Katsnelson and K. Novoselov, *Appl. Phys. Lett.*, 2013, **103**, 251607.
- 87 J. Y. Kwak, J. Hwang, B. Calderon, H. Alsalman, N. Munoz, B. Schutter and M. G. Spencer, *Nano Lett.*, 2014, **14**, 4511.
- 88 S. Bertolazzi, D. Krasnozhan and A. Kis, *ACS Nano*, 2013, **7**, 3246–3252.
- 89 M. S. Choi, G.-H. Lee, Y.-J. Yu, D.-Y. Lee, S. H. Lee, P. Kim, J. Hone and W. J. Yoo, *Nat. Commun.*, 2013, **4**, 1624.
- 90 H. S. Lee, S. W. Min, M. K. Park, Y. T. Lee, P. J. Jeon, J. H. Kim, S. Ryu and S. Im, *Small*, 2012, **8**, 3111–3115.
- 91 W. J. Yu, Z. Li, H. Zhou, Y. Chen, Y. Wang, Y. Huang and X. Duan, *Nat. Mater.*, 2013, **12**, 246–252.
- 92 K. Roy, M. Padmanabhan, S. Goswami, T. P. Sai, G. Ramalingam, S. Raghavan and A. Ghosh, *Nat. Nanotechnol.*, 2013, **8**, 826–830.
- 93 L. Britnell, R. Ribeiro, A. Eckmann, R. Jalil, B. Belle, A. Mishchenko, Y.-J. Kim, R. Gorbachev, T. Georgiou and S. Morozov, *Science*, 2013, **340**, 1311–1314.
- 94 M. Bernardi, M. Palummo and J. C. Grossman, *Nano Lett.*, 2013, **13**, 3664–3670.
- 95 D. Jariwala, V. K. Sangwan, C.-C. Wu, P. L. Prabhurashi, M. L. Geier, T. J. Marks, L. J. Lauhon and M. C. Hersam, *Proc. Natl. Acad. Sci. U. S. A.*, 2013, **110**, 18076–18080.
- 96 M. R. Esmaili-Rad and S. Salahuddin, *Sci. Rep.*, 2013, **3**, 2345.
- 97 Y. Deng, Z. Luo, N. J. Conrad, H. Liu, Y. Gong, S. Najmaei, P. M. Ajayan, J. Lou, X. Xu and P. D. Ye, *ACS Nano*, 2014, **8**, 8292–8299.
- 98 C.-H. Lee, G.-H. Lee, A. M. van der Zande, W. Chen, Y. Li, M. Han, X. Cui, G. Arefe, C. Nuckolls, T. F. Heinz, J. Guo, J. Hone and P. Kim, *Nat. Nano*, 2014, **9**, 676–681.
- 99 A. van der Zande, J. Kunstmann, A. Chernikov, D. Chenet, Y. You, X. Zhang, P. Y. Huang, T. C. Berkelbach, L. Wang and F. Zhang, *Nano Lett.*, 2014, **14**, 3869.
- 100 G. W. Shim, K. Yoo, S.-B. Seo, J. Shin, D. Y. Jung, I.-S. Kang, C. W. Ahn, B. J. Cho and S.-Y. Choi, *ACS Nano*, 2014, **8**, 6655.
- 101 J. S. Ross, P. Klement, A. M. Jones, N. J. Ghimire, J. Yan, D. Mandrus, T. Taniguchi, K. Watanabe, K. Kitamura and W. Yao, *Nat. Nanotechnol.*, 2014, **9**, 268–272.
- 102 B. W. Baugher, H. O. Churchill, Y. Yang and P. Jarillo-Herrero, *Nat. Nanotechnol.*, 2014, **9**, 262–267.
- 103 A. Pospischil, M. M. Furchi and T. Mueller, *Nat. Nanotechnol.*, 2014, **9**, 257.
- 104 M. P. Levendorf, C.-J. Kim, L. Brown, P. Y. Huang, R. W. Havener, D. A. Muller and J. Park, *Nature*, 2012, **488**, 627–632.
- 105 C. Huang, S. Wu, A. M. Sanchez, J. J. P. Peters, R. Beanland, J. S. Ross, P. Rivera, W. Yao, D. H. Cobden and X. Xu, *Nat. Mater.*, 2014, **13**, 1096.
- 106 X. Duan, C. Wang, J. C. Shaw, R. Cheng, Y. Chen, H. Li, X. Wu, Y. Tang, Q. Zhang, A. Pan, J. Jiang, R. Yu, Y. Huang and X. Duan, *Nat. Nano*, 2014, DOI: 10.1038/nnano.2014.222.
- 107 Y. Gong, J. Lin, X. Wang, G. Shi, S. Lei, Z. Lin, X. Zou, G. Ye, R. Vajtai, B. I. Yakobson, H. Terrones, M. Terrones, B. K. Tay, J. Lou, S. T. Pantelides, Z. Liu, W. Zhou and P. M. Ajayan, *Nat. Mater.*, 2014, **13**, 1135.
- 108 A. Kutana, E. S. Penev and B. I. Yakobson, *Nanoscale*, 2014, **6**, 5820–5825.
- 109 J. Mann, Q. Ma, P. M. Odenthal, M. Isarraraz, D. Le, E. Preciado, D. Barroso, K. Yamaguchi, G. V. Palacio, A. Nguyen, T. Tran, M. Wurch, A. Nguyen, V. Klee, S. Bobek, D. Z. Sun, T. F. Heinz, T. S. Rahman, R. Kawakami and L. Bartels, *Adv. Mater.*, 2014, **26**, 1399–1404.
- 110 Y. C. Lin, D. O. Dumcenco, H. P. Komsa, Y. Niimi, A. V. Krasheninnikov, Y. S. Huang and K. Suenaga, *Adv. Mater.*, 2014, **26**, 2857–2861.
- 111 I. S. Kim, V. K. Sangwan, D. Jariwala, J. D. Wood, S. Park, K.-S. Chen, F. Shi, F. Ruiz-Zepeda, A. Ponce, M. Jose-Yacaman, V. P. Dravid, T. J. Marks, M. C. Hersam and L. J. Lauhon, *ACS Nano*, 2014, **8**, 10551–10558.
- 112 C. H. Ho, C. S. Wu, Y. S. Huang, P. C. Liao and K. K. Tiong, *J. Phys.: Condens. Matter*, 1998, **10**, 9317–9328.
- 113 S. K. Srivastava, T. K. Mandal and B. K. Samantaray, *Synth. Met.*, 1997, **90**, 135–142.
- 114 Q. L. Feng, Y. M. Zhu, J. H. Hong, M. Zhang, W. J. Duan, N. N. Mao, J. X. Wu, H. Xu, F. L. Dong, F. Lin, C. H. Jin, C. M. Wang, J. Zhang and L. M. Xie, *Adv. Mater.*, 2014, **26**, 2648–2653.
- 115 D. O. Dumcenco, H. Kobayashi, Z. Liu, Y. S. Huang and K. Suenaga, *Nat. Commun.*, 2013, **4**, 1351.
- 116 B. Radisavljevic and A. Kis, *Nat. Mater.*, 2013, **12**, 815–820.
- 117 C. H. Ahn, J. M. Triscone and J. Mannhart, *Nature*, 2003, **424**, 1015–1018.
- 118 S. Tongay, J. Zhou, C. Ataca, J. Liu, J. S. Kang, T. S. Matthews, L. You, J. Li, J. C. Grossman and J. Wu, *Nano Lett.*, 2013, **13**, 2831–2836.
- 119 M. S. Fuhrer and J. Hone, *Nat. Nano*, 2013, **8**, 146–147.
- 120 B. Radisavljevic and A. Kis, *Nat. Nano*, 2013, **8**, 147–148.
- 121 S. Kim, A. Konar, W.-S. Hwang, J. H. Lee, J. Lee, J. Yang, C. Jung, H. Kim, J.-B. Yoo, J.-Y. Choi, Y. W. Jin, S. Y. Lee, D. Jena, W. Choi and K. Kim, *Nat. Commun.*, 2012, **3**, 1011.
- 122 H. Liu and P. D. Ye, *IEEE Electron Device Lett.*, 2012, **33**, 546–548.
- 123 W. Bao, X. Cai, D. Kim, K. Sridhara and M. S. Fuhrer, *Appl. Phys. Lett.*, 2013, **102**, 042104.
- 124 Z.-Y. Ong and M. V. Fischetti, *Phys. Rev. B: Condens. Matter Mater. Phys.*, 2013, **88**, 165316.
- 125 L. Zeng, Z. Xin, S. Chen, G. Du, J. Kang and X. Liu, *Appl. Phys. Lett.*, 2013, **103**, 113505.
- 126 M. M. Perera, M.-W. Lin, H.-J. Chuang, B. P. Chamlagain, C. Wang, X. Tan, M. M.-C. Cheng, D. Tomanek and Z. Zhou, *ACS Nano*, 2013, **7**, 4449–4458.
- 127 D. Jariwala, V. K. Sangwan, D. J. Late, J. E. Johns, V. P. Dravid, T. J. Marks, L. J. Lauhon and M. C. Hersam, *Appl. Phys. Lett.*, 2013, **102**, 173107.

- 128 V. K. Sangwan, H. N. Arnold, D. Jariwala, T. J. Marks, L. J. Lauhon and M. C. Hersam, *Nano Lett.*, 2013, **13**, 4351–4355.
- 129 L. Ming-Wei, L. Lezhang, L. Qing, T. Xuebin, S. D. Kulwinder, Z. Peng, M. N. Vaman, C. Mark Ming-Cheng and Z. Zhixian, *J. Phys. D: Appl. Phys.*, 2012, **45**, 345102.
- 130 Y. Li, C.-Y. Xu, P. Hu and L. Zhen, *ACS Nano*, 2013, **7**, 7795–7804.
- 131 S.-L. Li, K. Wakabayashi, Y. Xu, S. Nakaharai, K. Komatsu, W.-W. Li, Y.-F. Lin, A. Aparecido-Ferreira and K. Tsukagoshi, *Nano Lett.*, 2013, **13**, 3546–3552.
- 132 H. Fang, M. Tosun, G. Seol, T. C. Chang, K. Takei, J. Guo and A. Javey, *Nano Lett.*, 2013, **13**, 1991–1995.
- 133 S. Das, H.-Y. Chen, A. V. Penumatcha and J. Appenzeller, *Nano Lett.*, 2012, **13**, 100–105.
- 134 I. Popov, G. Seifert and D. Tománek, *Phys. Rev. Lett.*, 2012, **108**, 156802.
- 135 W. Liu, J. Kang, D. Sarkar, Y. Khatami, D. Jena and K. Banerjee, *Nano Lett.*, 2013, **13**, 1983–1990.
- 136 S. Walia, S. Balendhran, Y. Wang, R. Ab Kadir, A. Sabirin Zoofakar, P. Atkin, J. Zhen Ou, S. Sriram, K. Kalantar-zadeh and M. Bhaskaran, *Appl. Phys. Lett.*, 2013, **103**, 232105.
- 137 C. Gong, C. Huang, J. Miller, L. Cheng, Y. Hao, D. Cobden, J. Kim, R. S. Ruoff, R. M. Wallace, K. Cho, X. Xu and Y. J. Chabal, *ACS Nano*, 2013, **7**, 11350–11357.
- 138 J.-R. Chen, P. M. Odenthal, A. G. Swartz, G. C. Floyd, H. Wen, K. Y. Luo and R. K. Kawakami, *Nano Lett.*, 2013, **13**, 3106–3110.
- 139 H. Fang, S. Chuang, T. C. Chang, K. Takei, T. Takahashi and A. Javey, *Nano Lett.*, 2012, **12**, 3788–3792.
- 140 K. Ueno, S. Nakamura, H. Shimotani, A. Ohtomo, N. Kimura, T. Nojima, H. Aoki, Y. Iwasa and M. Kawasaki, *Nat. Mater.*, 2008, **7**, 855–858.
- 141 H. T. Yuan, H. Shimotani, A. Tsukazaki, A. Ohtomo, M. Kawasaki and Y. Iwasa, *Adv. Funct. Mater.*, 2009, **19**, 1046–1053.
- 142 K. Ueno, S. Nakamura, H. Shimotani, H. T. Yuan, N. Kimura, T. Nojima, H. Aoki, Y. Iwasa and M. Kawasaki, *Nat. Nanotechnol.*, 2011, **6**, 408–412.
- 143 Y. Yamada, K. Ueno, T. Fukumura, H. T. Yuan, H. Shimotani, Y. Iwasa, L. Gu, S. Tsukimoto, Y. Ikuhara and M. Kawasaki, *Science*, 2011, **332**, 1065–1067.
- 144 S. Asanuma, P. H. Xiang, H. Yamada, H. Sato, I. H. Inoue, H. Akoh, A. Sawa, K. Ueno, H. Shimotani, H. Yuan, M. Kawasaki and Y. Iwasa, *Appl. Phys. Lett.*, 2010, **97**, 142110.
- 145 H. T. Yuan, M. S. Bahramy, K. Morimoto, S. F. Wu, K. Nomura, B. J. Yang, H. Shimotani, R. Suzuki, M. Toh, C. Kloc, X. D. Xu, R. Arita, N. Nagaosa and Y. Iwasa, *Nat. Phys.*, 2013, **9**, 563–569.
- 146 Y. J. Zhang, J. T. Ye, Y. Matsushashi and Y. Iwasa, *Nano Lett.*, 2012, **12**, 1136–1140.
- 147 Y. J. Zhang, J. T. Ye, Y. Yornogida, T. Takenobu and Y. Iwasa, *Nano Lett.*, 2013, **13**, 3023–3028.
- 148 D. Braga, I. Gutiérrez Lezama, H. Berger and A. F. Morpurgo, *Nano Lett.*, 2012, **12**, 5218–5223.
- 149 K. Ueno, H. Shimotani, H. T. Yuan, J. T. Ye, M. Kawasaki and Y. Iwasa, *J. Phys. Soc. Jpn.*, 2014, **83**.
- 150 J. T. Ye, Y. J. Zhang, R. Akashi, M. S. Bahramy, R. Arita and Y. Iwasa, *Science*, 2012, **338**, 1193–1196.
- 151 S. F. Wu, J. S. Ross, G. B. Liu, G. Aivazian, A. Jones, Z. Y. Fei, W. G. Zhu, D. Xiao, W. Yao, D. Cobden and X. D. Xu, *Nat. Phys.*, 2013, **9**, 149–153.
- 152 H. Yuan, X. Wang, B. Lian, H. Zhang, X. Fang, B. Shen, G. Xu, Y. Xu, S.-C. Zhang, H. Y. Hwang and Y. Cui, *Nat. Nano*, 2014, **9**, 851–857.
- 153 S. Tarasenko, *Nat. Nanotechnol.*, 2014, **9**, 752–753.
- 154 H. Yu, Y. Wu, G.-B. Liu, X. Xu and W. Yao, *Phys. Rev. Lett.*, 2014, **113**, 156603.
- 155 A. P. Nayak, S. Bhattacharyya, J. Zhu, J. Liu, X. Wu, T. Pandey, C. Q. Jin, A. K. Singh, D. Akinwande and J. F. Lin, *Nat. Commun.*, 2014, **5**.
- 156 X. D. Xu, W. Yao, D. Xiao and T. F. Heinz, *Nat. Phys.*, 2014, **10**, 343–350.
- 157 W. Yao, D. Xiao and Q. Niu, *Phys. Rev. B: Condens. Matter Mater. Phys.*, 2008, **77**, 235406.
- 158 D. Xiao, G. B. Liu, W. X. Feng, X. D. Xu and W. Yao, *Phys. Rev. Lett.*, 2012, **108**, 196802.
- 159 M. Ezawa, *Phys. Rev. B: Condens. Matter Mater. Phys.*, 2012, **86**, 161407.